DYNAMIC PRECIPITATION OF SECOND PHASE UNDER DEFORMED CONDITION IN Mg-Nd BASED ALLOY

Nilesh Bajirao Dendge

Thesis Prepared for the Degree of

MASTER OF SCIENCE

UNIVERSITY OF NORTH TEXAS

December 2013

APPROVED:

Rajarshi Banerjee, Major Professor
Rajiv Mishra, Committee Member
Narendra Dahotre, Committee Member and Chair of the Department of Materials Science and Engineering
Costas Tsatsoulis Dean of the College of Engineering
Mark Wardell, Dean of the Toulouse Graduate School

Dendge, Nilesh Bajirao. Dynamic Precipitation of Second Phase Under Deformed Condition in Mg-Nd Based Alloy. Master of Science (Materials and Science Engineering), December 2013, 60 pp., 3 tables, 34 figures, references, 47 titles.

Magnesium alloys are the lightweight structural materials with high strength to weigh ratio that permits their application in fuel economy sensitive automobile industries. Among the several flavors of of Mg-alloys, precipitation hardenable Mg-rare earth (RE) based alloys have shown good potential due to their favorable creep resistance within a wide window of operating temperatures ranging from 150°C to 300°C. A key aspect of Mg-RE alloys is the presence of precipitate phases that leads to strengthening of such alloys. Several notable works, in literature, have been done to examine the formation of such precipitate phases. However, there are very few studies that evaluated the effect stress induced deformation on the precipitation in Mg-RE alloys.

Therefore, the objective of this work is to examine influence of deformation on the precipitation of Mg-Nd based alloys. To address this problem, precipitation in two Mg-Nd based alloys, subjected to two different deformation conditions, and was examined via transmission electron microscopy (TEM) and atom probe tomography (APT).

In first deformation condition, Md-2.6wt%Nd alloy was subjected to creep deformation (90MPa / 177ºC) to failure. Effect of stress-induced deformation was examined by comparing and contrasting with precipitation in non-creep tested specimens subjected to isothermal annealing (at 177ºC). In second condition, Mg-4.0Y-3.0Nd-0.5Zr (wt %) or WE43 alloy (with comparable Nd content as model Mg-Nd system) was subjected to hot rolling deformation at a sub-solvus temperature.

ACKNOWLEDGEMENTS

First and foremost, I offer my sincerest gratitude to my advisor, Prof. Rajarshi Banerjee, who has supported me throughout my thesis with his patience and immense knowledge whilst providing me the opportunity and confidence to work in my own way.

Besides my advisor, I would like to thank thesis committee: Prof. Narendra Dahotre and Prof. Rajiv Mishra for their encouragement and insightful comments.

I am also very thankful to Dr. Deep Choudhuri and Dr. Soumya Nag for their support and guidance in learning new instruments, and running experiments. I am grateful to my fellow labmates, who not only made my daily work fun but also provided me with valuable insights to my research work. I would also like to thank all the members of CART for facilitating the use of instruments.

My gratitude also goes to all other professors of materials science department for stimulating discussions during courses, and their valuable feedback whenever requested.

Finally, I thank my parents and siblings for supporting and encouraging me throughout my stay at University of North Texas.

TABLE OF CONTENTS

Page

LIST OF TABLES

Page

LIST OF FIGURES

Page

CHAPTER 1

INTRODUCTION

1.1 History

Magnesium has been used in our history, during WWI & WWII, for applications in the nuclear industry, metal and aircraft, the significance of which declined afterward. Nowadays, magnesium-based alloys have found application as a structural material in automobile, aircraft and electronics (potentially) industries. The recent use of magnesium in the VW beetle is the most significant application. .

Light weight of magnesium alloys attracts automobile manufacture to replace denser materials such as steels, cast irons, copper alloys and aluminum alloys. It also has the highest strength-to-weight ratio compared to any other of commonly used metals. In addition, many other advantages of magnesium (e.g., good castability, high die casting rates, electromagnetic interference shielding properties, parts consolidation, dimensional accuracy, and excellent machinability) encourage the utilization of this interesting lightweight metal in the automotive industry [1].

1.2. Alloy Design

Based on property requirement for particular application, alloy developments were needed. Such a application oriented alloy selection is schematically depicted in Figure 1 [2]. The following subsections will discuss alloys used in practical application.

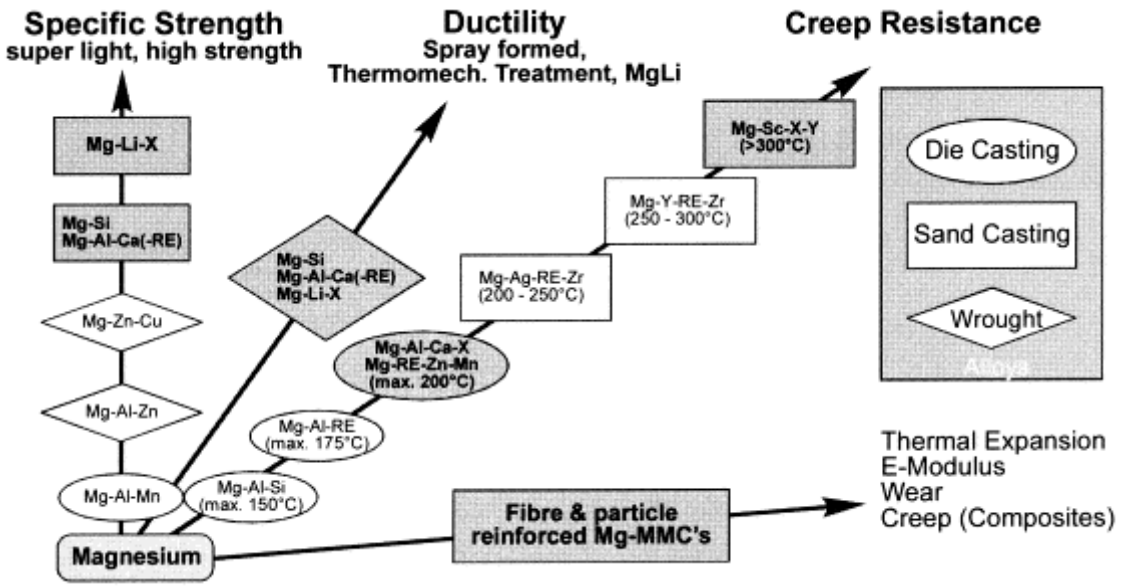

Figure 1 Classification of Alloy Development

I. Specific Strength

The commercial alloy AZ91 is used for numerous applications. This alloys is subjected to application with temperature lower than 130°C due to its poor creep resistance. The alloying addition to magnesium improves the specific strength and delay its over ageing. Because of its high specific strength, it used as automobile components, constructional part etc. The alloy systems for high specific strength are Mg-Al, Mg-Al-Mn, Mg-Al-Zn, Mg-Si, Mg-Al-Ca (RE) etc.

II. Ductility

This property is needed for alloys with capability of high ductility under thermo mechanical treatment. Magnesium has hexagonal crystal structure. Because of its structure, there are limited slip systems. The low ductility can be changed by addition of alloying elements. The alloy system for instance Mg-Si, Mg-Al-Ca (RE), and Mg-Li-X develops phase mixture of bcc & hcp phases. This helps to improve ductility of alloy.

III. Creep Resistance

HZ22 alloy with thorium addition perform at the highest service temperature of magnesium (i.e. 623K) compared to melting point of magnesium. The radioactivity of thorium expel as an alloying elements. For powertrain application, there is need of alloy with high creep resistance. There are various service temperature e.g. 150°C, 170°C, 200°C. In previous work, rare earth (RE) alloying element addition to magnesium alloy was suggested to improve creep resistance. This part will be further discussed in section 3 of this chapter.

IV. Fiber and particle reinforced magnesium (MMCs)

To improve certain properties of magnesium, the reinforcement materials such as Al_2O_3, SiC, or carbon are used. This reinforcement help to improve elastic modulus wear resistance or thermal expansion [ref].

1.3. Mg-RE Alloys

For application at high temperature, the addition of alloying element such as RE (Nd, Gd La etc [3], Y & Sc is used to enhance creep resistance properties. Presence of RE elements permits precipitation of hardening phases within α-Mg matrix upon annealing. The precipitation sequence in different Mg-RE alloy is shown as below [4]. The precipitation sequence and phase morphology may depend not only on alloy composition but also on casting technology and thermo mechanical treatment. The mechanical properties depend on phase morphology, volume fraction and arrangement of these phases.

As indicated in Table I, several studies have been carried out to determine the precipitate phases present in Mg-RE based alloys [5, 6]. However, most of these studies examined precipitate phase by isothermally annealing a solutionized microstructure (free of precipitation within the initial microstructure). So far there has been limited work to investigate precipitation within α-Mg matrix that experienced prior deformation, or during deformation (dynamic

precipitation). Application external stress, to cause deformation, results in elastic and plastic (due to dislocations) strains within the parent α-Mg matrix. It is possible that such stresses may interact with the transformation strains of precipitate phases and enhance their formation in α-Mg. Therefore, the objective of this work is to examine influence of deformation on the precipitation of the Mg-RE based alloys. To address this problem, precipitation in two Mg-Re based alloys, subjected to two different deformation conditions, was examined via transmission electron microscopy (TEM) and atom probe tomography (APT):

1. Md-2.6wt%Nd: A model alloy, subjected to creep deformation (90MPa / 177ºC) to failure. Effect of stress-induced deformation was examined by comparing and contrasting with precipitation in non-creep tested specimens subjected to isothermal annealing (at 177ºC).
2. Mg-4.0Y-3.0Nd-0.5Zr (wt %) or WE43: A commercial alloy (with comparable Nd content as model Mg-Nd system) subjected to hot rolling deformation at a sub-solvus temperature.

Table 1. Summary of precipitate phases present in Mg-Nd and Mg-Y-Nd alloys systems [7]

Mg-Nd	super saturated solid solution (SSSS)	GP zone	β″ DO_{19} hexagonal plates a=2a_{Mg}, c=c_{Mg} (0001 $_{β″}$ ‖(0001)$_{Mg}$ [2-1-10]$_{β″}$‖[2-1-10]$_{Mg}$	β′ orthorhombic, a=0.64 nm, b=1.11 nm, c= 0.52nm [100]$_{β′}$ ‖ [11-20]$_{Mg}$, [010]$_{β′}$ ‖ [-1100]$_{Mg}$, and (001)$_{β′}$ ‖ (0001)$_{Mg}$	$β_1$ fcc a=0.736 nm (011) $_{β1}$ ‖(0001)$_{Mg}$ (-11-1)$_{β1}$‖(-2110)$_{Mg}$	β tetragonal incoherent a=1.03 nm c=0.593 nm	βe tetragonal a=1.47nm , c=1.04nm
Mg-Y-Nd	SSSS	GP zone	β″ DO_{19} hexagonal plates a=2a_{Mg}, c=c_{Mg} (0001) $_{β″}$ ‖(0001)$_{Mg}$ [2-1-10] $_{β″}$‖ [2-1-10]$_{Mg}$	β′ orthorhombic a=0.640nm,b=2.223, c=0.521nm (100) $_{β′}$ ‖(1-210)$_{Mg}$, [001]) $_{β′}$ ‖[0001]$_{Mg}$	$β_1$ fcc a=0.74 nm (-112) $_{β1}$ ‖(1-100)$_{Mg}$, [110] $_{β1}$ ‖[0001]$_{Mg}$		β fcc a=2.20nm incoherent

CHAPTER 2

EXPERIMENTAL DETAILS

2.1. Alloy System

2.1.1. Mg-2.6Nd (wt%)

All specimens were received in the form of dog - bone shaped tensile bar. These specimens were cast in high-pressured die cast (250 tonne) Toshiba (Toshiba Machine Co. Company, Japan) horizontal cold chamber die casting machine. The dimensions of specimen are as follows: total length = 100 mm, gauge length = 32 mm, and gauge diameter = 5.6 mm. The nominal composition of this alloy is Mg-2.6Nd (in weight percent). Creep tests were performed at a nominal uniaxial stress of 90 MPa in an oil bath maintained at 177°C. These tests were carried out in three conditions i.e. 5hrs, 100hrs, and creep tested to failure ~230hrs. Simultaneously, other set, of the same alloy, were isothermally aged at 177°C for 5hrs, 100hrs, and 230hrs corresponding to creep tested conditions

2.1.2 Commercial WE43 alloy: Mg-3Y-4Nd-0.5Zr (wt %)

5.25 mm thick hot-rolled plate of WE43 alloy were supplied by Magnesium Electron North America, Inc. The WE43 alloy in cast condition were solutionized at 525°C for 8 hrs and quenched in water. After solutionizing, WE43 alloy were hot rolled to achieve 95% thickness reduction at a commercially proprietary sub-solvus temperature, which was done at Magnesium Electron North America, Inc. The nominal composition of WE43 alloy is Mg -4.0 Y-3.3 Nd -0.5 Zr (in weight percent).

2.2. Characterization Tools

2.2.1. Scanning Electron Microscope (SEM)

In order to study microstructure, a SEM technique has been used in these alloy system. The FEI Sirion^{TM} FEG instrument operating at (5KeV- 30KeV) has been used. This instrument was aided with Field emission gun (FEG). The other features of this instrument were Back scattered detector (BSE), Everhart Thornley Detector (ETD) i.e. secondary electrons detector and Through Lens Detector (TLD). The energy dispersive spectrometer (EDS) and electron backscattered diffraction (EBSD) was equipped to this instrument for chemical composition measurement and orientation mapping respectively. The images were captured using secondary electron mode, and backscattered electron mode. To achieve high quality image, immersion mode was used with above-mentioned modes.

2.2.2. Focused Ion Beam (FIB)

The FEI dual beam focused ion beam (Nova Nanolab 200^{TM}) system was utilized to prepare site-specific samples for transmission electron microscope and / or 3D atom probe studies. This instrument was equipped with two modes. One was secondary electron mode and other was ion mode (gallium ion). The surrounding area of interest in sample was exposed to ion mode. In this mode, accelerated gallium ion milled out surrounding area of interest. Once appropriate size of specimen was prepared and lift out in-situ with help of omniprobe manipulator, equipped with instrument.

The rectangular shape (30 μm × 10 μm × 3 μm) of lift out was attached to copper grid placed in microscope for TEM samples. The top surface of sample was usually coated with platinum to protect sample from gallium ions. The attached sample was milled to thickness,

which looked like electron transparent. The appropriate voltage and current values were used to minimize sample damage by gallium ions.

Samples for 3D atom probe were prepared in a slightly different way compared to mention above. FIB was used to make sharp tip (tip radius ≤ 100nm). Placing rectangular block of lift out on the top of post, these tips were prepared. This post made up of silicon and has a pillar shape with flat circular region on the pillar. The blocks on the post were milled to shape of cone with desired tip radius.

2.2.3. Transmission Electron Microscope (TEM)

Transmission electron microscope was used to identify and characterize precipitate that was quite difficult to perform with SEM. The FEI Tecnai F20^{TM} FEG operating at 200KV was used to study samples. TEM examination was carried out in conventional, high resolution (HRTEM) and high angle annular dark field scanning TEM (HAADF-STEM) modes .

2.2.4. 3D Atom Probe Tomography

The three-dimensional atom probe (LEAP 3000X HR) was used for near atomic resolution determination of the elemental identities and spatial coordinated of individual atom within a small volume [8]. The voltage pulses mode and laser beam mode was used to evaporate atoms in form of ions from the tips of specimen. The collected data was used to reconstruction of evaporated volume by using IVAS software. The chemical identification of ions was determined based on their measure time of flight from the tip of specimen to the detector. The time of flight for different ions varies with their mass to charge ratio. The spatial coordinates of ion were determined by the encoded impact position on position sensitive detector. For above-mentioned alloys, atom probe study was conducted in a voltage evaporation mode with evaporation rate 0.5-

1.0%, pulsing voltage 20%, pulse rate 200Khz under high vacuum (~10^{-10} bar) at 50K. The collected data was analyzed using IVAS software.

CHAPTER 3

STRESS INDUCED DYNAMIC PRECIPITATION IN MG-ND ALLOY

3.1. Introduction And Motivation

Precipitation hardenable Mg-rare earth (RE) elements are potential candidates for automotive powertrain applications [3, 10, 11]. Mg-RE alloys have favorable creep properties, which permits a wide window of operating temperature ranging from 150ºC -300ºC [3-12-15].

The precipitates form dynamically within the stressed α-Mg matrix in the binary high-pressure die cast (HPDC) Mg-Nd alloys [3, 15]. The coupled influence of both temperature and applied stress on precipitation has been suggested. In addition, time also plays a role in precipitate evolution during creep [3, 12-15]. Thus, the dynamic precipitation becomes a function of applied stress, temperature and time.

Mg-Nd was chosen for two reasons: (i) it is a model template for several Mg-Nd based commercial alloys e.g. WE43 and WE54 (Mg-Nd-Y) [16-18], and (ii) it typically exhibits better creep properties than other binary Mg-La and Mg-Ce alloys [3]. This article will focus on determining the factors contributing to the dynamic precipitation in HPDC Mg-Nd subjected to creep.

In recent studies, the influence of temperature and time on the precipitation of Mg-Nd alloys has been examined [11, 18-20]. Based on previous literature, the precipitation sequence within the α-Mg matrix is as follows [19, 20]: GP zones $\rightarrow$ β″ (*DO_{19}*, Mg_3Nd) $\rightarrow$ β′ (*orthorhombic*, Mg_7Nd) $\rightarrow$ β_1 (*fcc* , Mg_3Nd) $\rightarrow$ β (*tetragonal*, $Mg_{12}Nd$) $\rightarrow$ β_e (*tetragonal*, $Mg_{41}Nd_5$, equilibrium phase). The metastable phases (GP zones, β″, β′ and β_1) are often observed in this alloy [13, 20], while high temperature annealing (e.g. 500ºC) for prolonged time is required to form β and the more stable β_e [11].

According to previous articles, the most of these studies have been performed on solutionized alloy. In contrast, a typical microstructure of HPDC contains α-Mg dendrites and interdendritic Mg_3Nd precipitates [11]. In HPDC, the defects formed within α -Mg grains, which provide as heterogeneous nucleation sites. These sites are subsequently decorated with precipitates during the annealing process [16]. Therefore, an evaluation of the temperature / time influence on precipitation in an HPDC alloy is worthy of further investigation.

The aim of this work is to separate the effect of applied stress on the precipitation process in binary Mg-Nd alloys by comparing isothermally annealed alloys with alloys subjected to creep deformation at the same temperature and for similar time periods. The differences in the precipitation behavior during creep versus isothermal annealing conditions have been investigated in detail by coupling transmission electron microscopy (TEM) and 3D atom tomography.

3.2. Experimental Procedure

All specimens were received in the form of dog - bone shaped tensile bar. These specimens were cast in high-pressured die cast (250 tonne) Toshiba (Toshiba Machine Co. Company, Japan) horizontal cold chamber die casting machine. The dimensions of specimen are as follows: total length = 100 mm, gauge length = 32 mm, and gauge diameter = 5.6 mm. The nominal composition of this alloy is Mg-2.6Nd (wt %). Creep tests were performed at a nominal uniaxial stress of 90 MPa in an oil bath maintained at 177°C. The oil bath was used to avoid oxidation of alloy. These tests were carried out in three conditions i.e. 5hrs, 100hrs, and creep tested to failure ~230hrs. Simultaneously, other sets of same materials were isothermally aged at 177°C for 5hrs, 100hrs, and 230hrs corresponding to creep tested conditions.

Using backscattered electron mode, microstructures of this alloy were obtained in the SEM. The FIB technique was used to prepare lift out. The lift out was taken from the cross section of dog bone shaped sample. The plane of TEM sample was parallel to loading direction of creep. Similarly, atom probe samples (APT) were prepared using FIB. The detail of procedure is explained in the chapter 2

3.3. Result

3.3.1. Creep Behavior

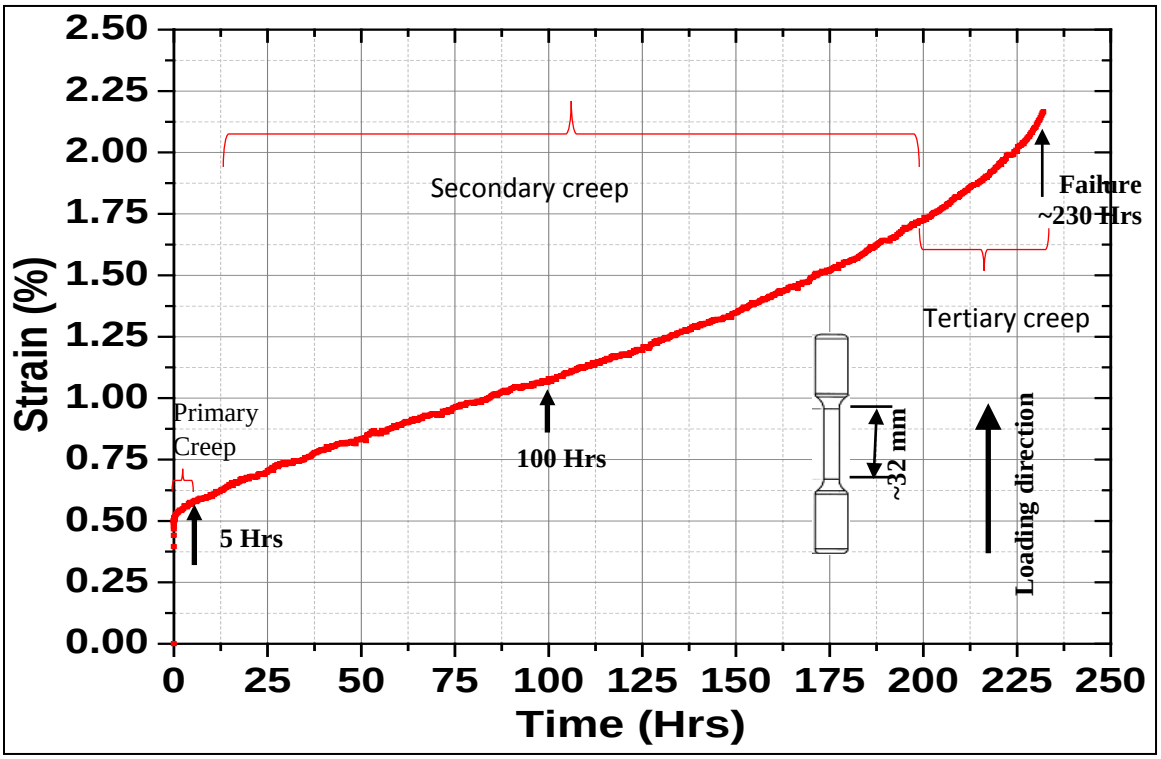

Figure 2 Strain vs time creep curve

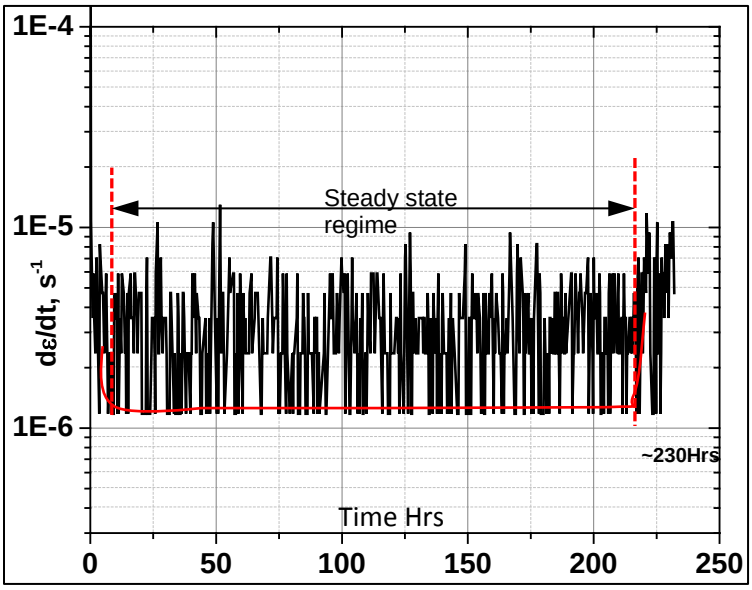

Figure 3 Strain rate vs time creep curve

The creep test was performed on dog bone shaped specimen for 90 MPa loading at 177°C. The creep behavior of this material is shown in Figure 2. The Figure 2 represent plot of strain vs time. The Figure 3 shows plot of strain rate versus time to determine different creep regimes. The steady state regime was found at approximately 3.4×10^{-6} s^{-1}. The extent of steady state regime is indicated in Figure 3. The primary and tertiary creep was found to be minimal. The samples were taken from 5hrs, 100hrs & 230hrs (failure) creep test.

3.3.2. As Cast Microstructure

As cast HPDC microstructure is shown in Figure 4a. The microstructure consists of inter-dendritic precipitate network surrounding α-Mg matrix. The SAD pattern was obtained from α-Mg matrix along [0001] zone axis to determine presence of intra-granular precipitates in α-Mg matrix region (Figure 4b). The absence of precipitate reflections from α-Mg matrix region indicates that these regions are largely free of precipitates in the as cast microstructure. The

formation of second phase precipitates in creep tested and isothermally annealed samples will compare in the next few sections.

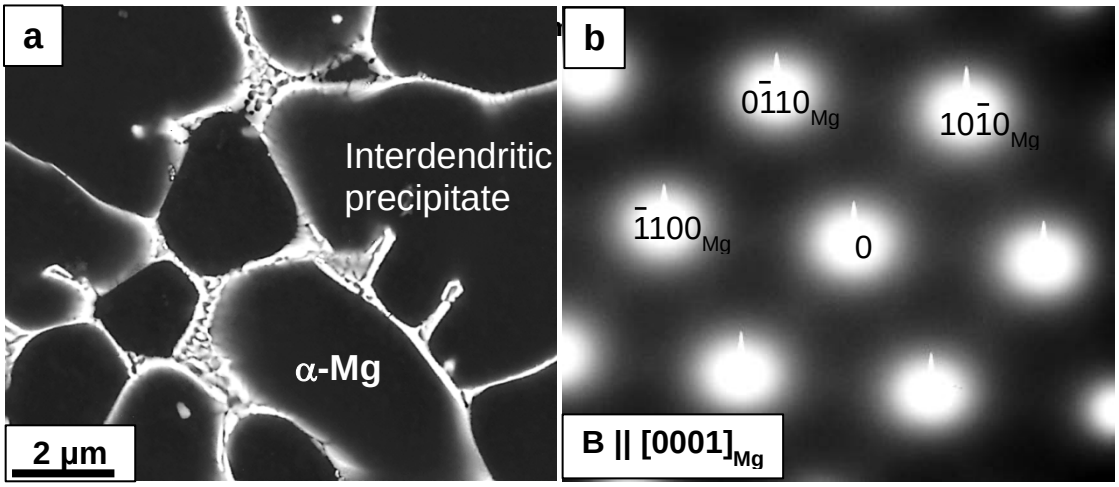

Figure 4 (a) As cast HPDC microstructure (b) SAD patter [0001] zone axis from α-Mg

3. 3.3. Early Stage Of Precipitation During Creep And Isothermal Annealing (~5 hrs)

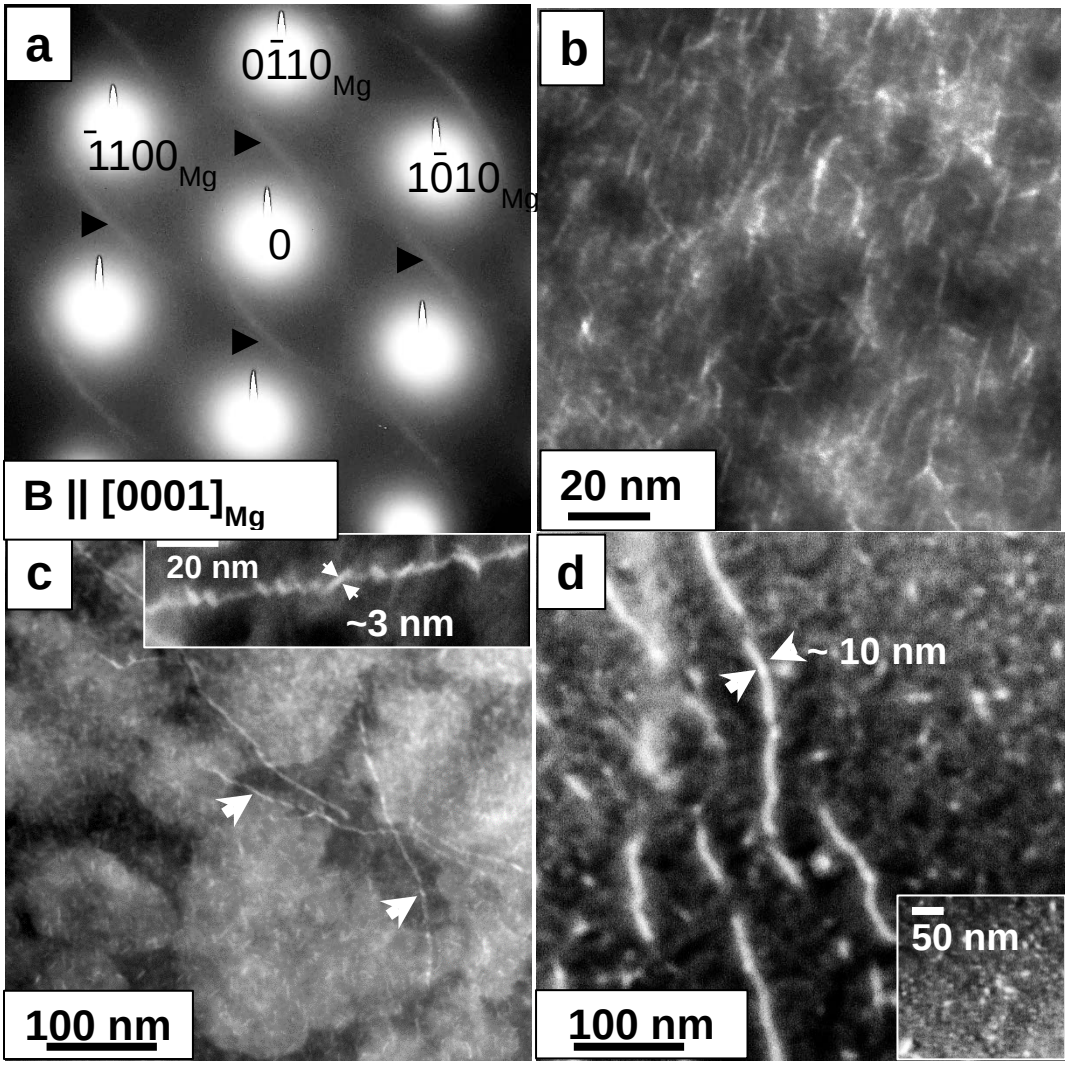

Figure 5 (a) SAD pattern along [0001] zone axis (b) HAADF-STEM showing β'(5 hrs creep tested sample) (c) HAADF- STEM showing curve trajectory precipitate (5 hrs creep tested sample) d) curve trajectory precipitate (5 hrs isothermally annealed)

The early stages of precipitation from 5 hrs creep tested sample and 5 hrs isothermally annealed samples are shown in Figure 5. The microstructure of 5 hrs creep tested sample showed fine scale precipitates. The SAD pattern along [0001] zone axis shows faint streaking (marked by arrow) passing through ½$\{10\text{-}10\}_{Mg}$ and ½$\{11\text{-}20\}_{Mg}$ positions (Figure 5a). The High Angle Annular Dark Field-scaning TEM (HAADF-STEM) imaging was performed with beam parallel to $[0001]_{Mg}$ zone axis to reveal the precipitates in the creep tested samples (Figure 5b and 5c). These Figures show two types of precipitate morphologies. (i) The Figure 5b shows

homogenously distributed extremely fine irregular thread like fragments [~10-15nm] throughout the matrix. (ii) The Figure 5c shows coarser plate like segments that seem to lie on dislocation lines (single trajectory) possibly with preferential alignment (Figure 5c inset). Based on HAADF-STEM image, volume fraction of plate like segments decorating dislocation lines seem to be lower compared with thread like fragments.

In case of 5 hrs isothermally annealed samples, the behavior of precipitation was different than 5 hrs creep tested samples. These differences are clearly seen by comparing Figure 5d of isothermally aged samples with Figure 5b and Figure 5c of creep tested samples. Pockets of localized Nd enrichment regions (~5-10nm) were observed exhibiting a bright contrast in Figure 5d. Saito and Hiraga reported that these Nd enrichment regions are likely to be GP zones formed with α-Mg matrix [5].

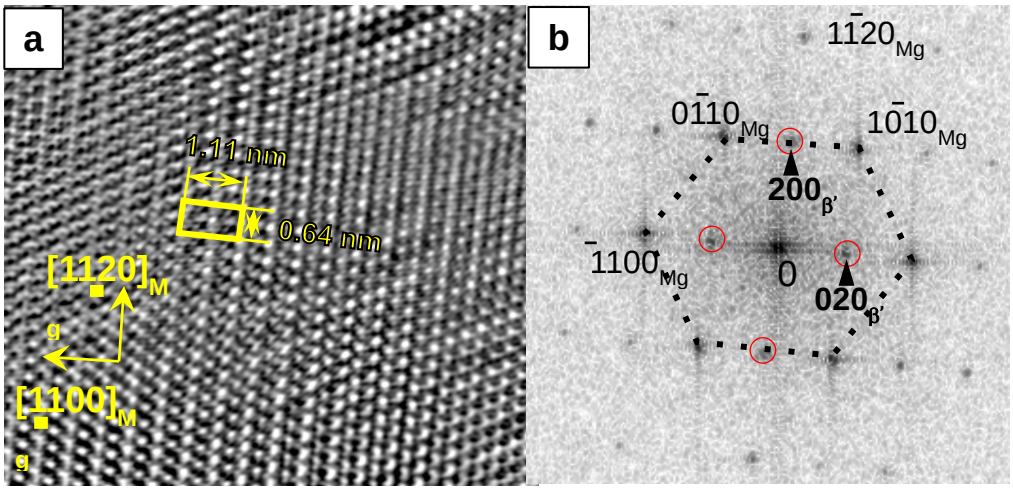

Figure 6 (a) HRTEM image of 5 hrs creep tested sample (b) FFT of 5 hrs creep tested sample

In addition to localized Nd enrichment regions in 5 hrs isothermal annealed samples, plates like precipitate forming on dislocation lines are observed (Figure 5d). The preferential alignments of plate like precipitate were not observed in 5 hrs isothermally annealed sample.

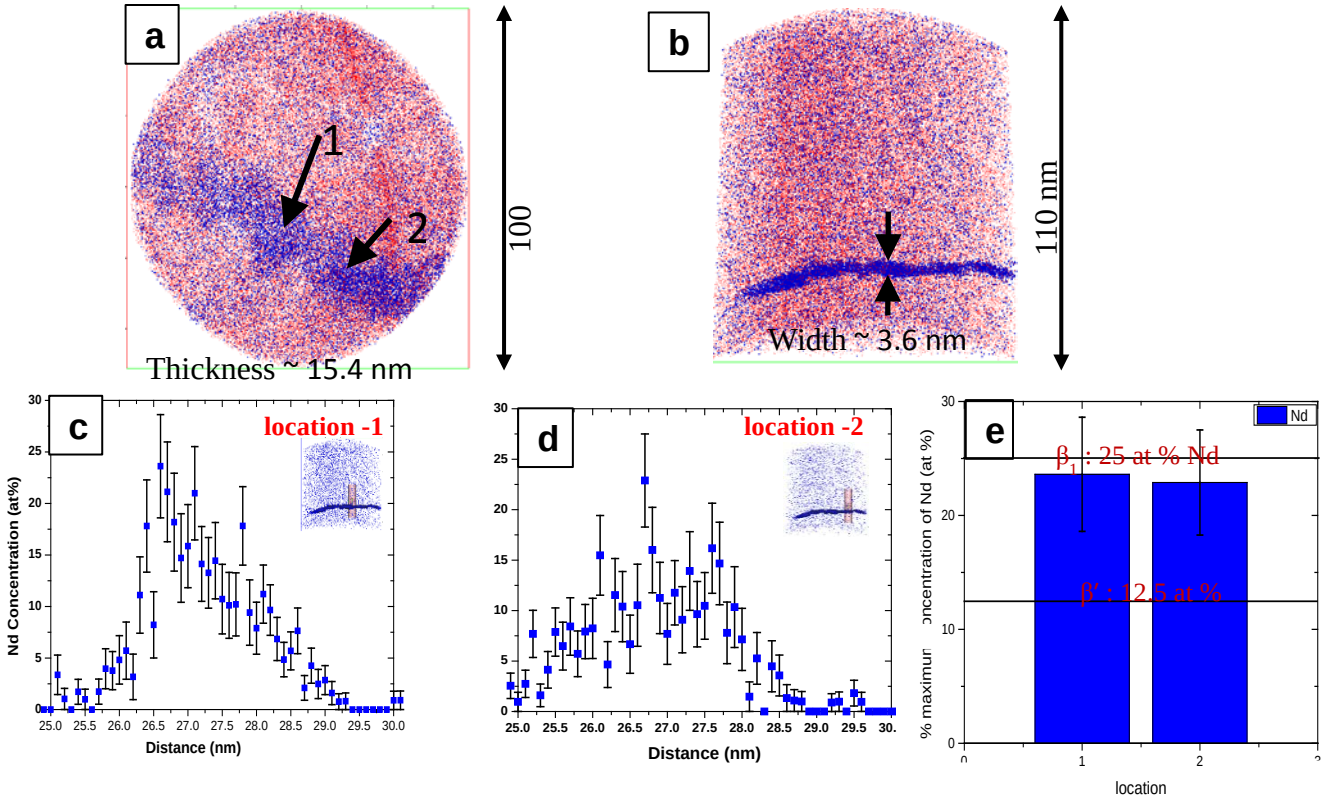

Figure 7 (a) 3D reconstruction with orthogonal view for 5 hrs aged (b) 3D reconstruction with side view 5hrs aged (c) ROI at location 1 (d) ROI at location 2 (e) maximum Nd concentration v/s location from ROI data

In order to determine structure of precipitates, high resolution TEM and corresponding fast fourier transform of 5 hrs creep tested samples were performed along $[0001]_{Mg}$ (Figure 6). The fast Fourier transform (FFT) diffraction pattern was obtained from a macroscopic area containing fine thread like fragments (Figure 6b). In the FFT, precipitates reflections at ½$\{10\text{-}10\}_{Mg}$ and ½$\{11\text{-}20\}_{Mg}$ location corresponded to (020) and (200) planes of β′ phase (Figure 6b) (orthorhombic, a = $2a_{Mg}$ = 0.64 nm, b= $2\sqrt{3}a_{Mg}$ = 1.11 nm, and c = c_{Mg} = 0.52 nm [5]. The HRTEM shows a (001) β′ plane motif marked with a and b lattice parameter (Figure 6a). Based on FFT (Figure 6b) and HRTEM image (Figure 6a), the orientation relationship of β′ and α-Mg matrix were obtained as $[100]_{\beta'} \parallel [11\text{-}20]_{Mg}$, $[010]_{\beta'} \parallel [\text{-}1100]_{Mg}$, and $(001)_{\beta'} \parallel (0001)_{Mg}$ which is

consistent with previous report in literature[5,6]. Therefore, the thread like precipitates in Figure 5c can be identified as β′ phase.

The atom probe tomography (APT) was used to determine composition of these precipitates. The Figure 7 shows APT results of 5hrs isothermally annealed sample. The Mg ions and Nd ions are indicated by red and blue colors respectively. The precipitate with curved trajectory showed in two different views as seen in Figure 7a and 7b. The morphology and size scale of precipitates observed in the 3D reconstruction matches with the precipitates in HAADF-STEM image (fig 5d). The cylindrical region of interest (ROI) was used to measure one dimensional concentration profile of precipitate. The one-dimensional concentration profile was measured using ROI at two different positions shown in Figure 7a. The Figures 7c and 7d showed one-dimensional concentration of Nd ions vs distance at location 1 & 2 respectively. The Figure 7e shows plot of the maximum Nd (at %) 1D concentration versus locations of ROI. The maximum 1D concentration of Nd ion at locations 1 and 2 observed approximately 23.75 at% Nd and 23 at % Nd respectively (Figure 7e). The composition of Nd ion in this precipitate is very close to β_1 precipitates i.e. Mg_3Nd (~25 at %).

Figure 8 shows local Nd enriched region in 5 hrs isothermally annealed sample. The different views of 3D reconstruction in the Figure 8a and 8b show fine-scaled local Nd enriched region. The calculation of localized Nd enriched region appears to be difficult to determine using proxigram or ROI method. Nevertheless, based on ROI method, the average composition of these Nd rich region is 3.01 ± 0.10 at % Nd.

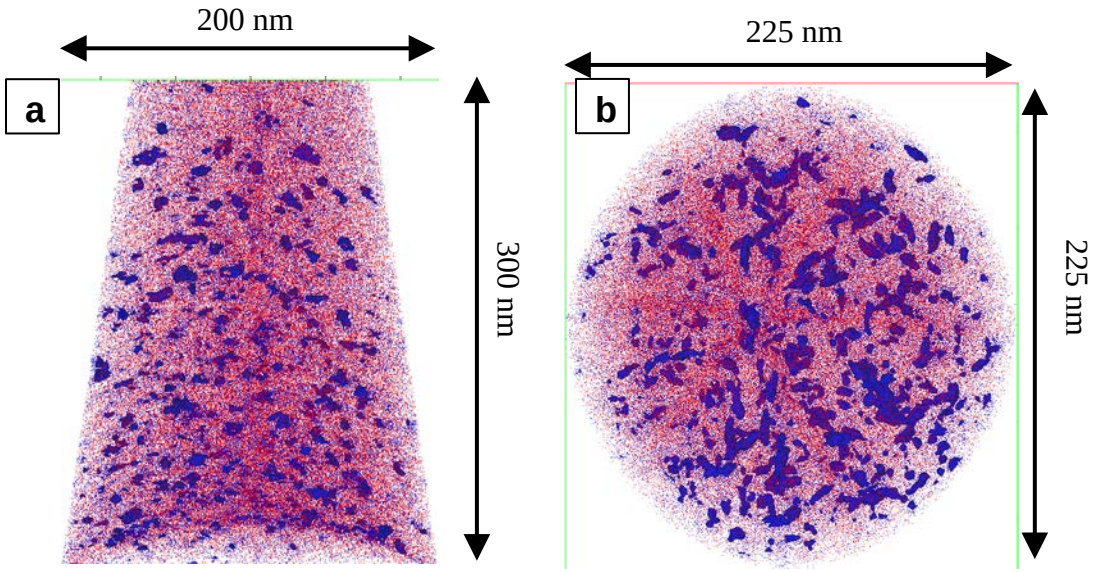

Figure 8 (a) 3D reconstruction from side view in 5 hrs isothermally annealed sample (b) 3D reconstruction from orthogonal view

Based on TEM (Figures 5c and 5d) and APT (Figures 7 and 8), plate like precipitate decorating dislocation lines are very likely to be β_1 (fcc, a = 0.74 nm) precipitates. Firstly, the size scale of plate like precipitates is much larger than the reported sizes of β" and β' precipitates. Secondly the morphology of β_1 is different than β' precipitates (Figure 5d). The formation of equilibrium β precipitate in early stages of creep testing and isothermal annealing is very difficult. Therefore, it can be identified as β_1 precipitate.

Form above mentioned results; it can be summarized as follow

1. The homogeneous distribution of thread like β' precipitates were observed in 5 hrs creep tested sample. In contrast, formations of localized Nd enriched regions were seen in 5 hrs isothermal annealing. According to literature, formation of local Nd enrichment and GP zones are always preceded β' formation. Creep seems to accelerate formation of β' precipitates homogeneously.
2. The plates like precipitate decorating dislocation lines were observed in both conditions. In creep tested condition, β_1 precipitates were preferentially aligned. However, β_1

precipitate in isothermally annealed condition did not show any kind of alignment. In isothermally annealed condition, the thickness (~15 nm) of β_1 precipitate (plate shaped) is greater that creep tested condition (~3nm).

3.3.4. Intermediate Stage Of Precipitation During Creep And Isothermally Annealing (~100 hrs)

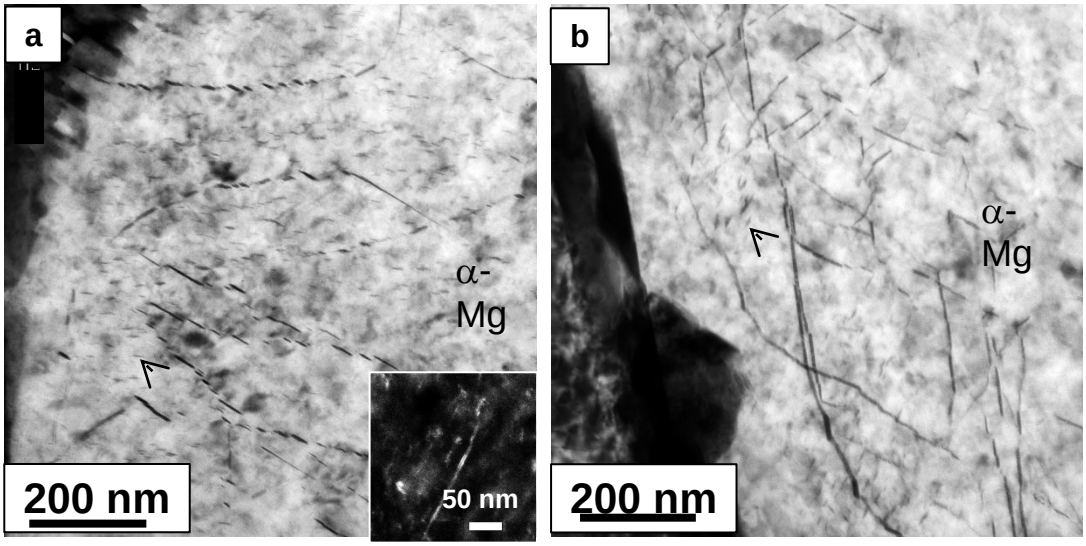

Figure 9 (a) Bright field image of 100 hrs creep tested sample (b) bright field image of 100 hrs isothermally annealed sample

The Figure 9a and 9b shows bright field TEM image of 100 hrs creep tested and 100 isothermally annealed creep tested samples respectively. Both Figures show inter-dendritic precipitation in α-Mg matrix. Elongated precipitates lies on curved trajectory are observed in both images. The inset in Figure 9a shows dark field image of one precipitate with elongated morphology. The corresponding SAD on $[0001]_{Mg}$ axis showed in Figures 10a and 10b for creep sample and isothermally annealed sample. The reflections marked in Figures 10a and 10b were indexed as β_1 precipitate for both conditions [7]. Therefore, β_1 precipitates were observed in creep tested and isothermally annealed condition. The morphology of β_1 precipitates appears to be elongated in both isothermally annealed and creep tested condition.

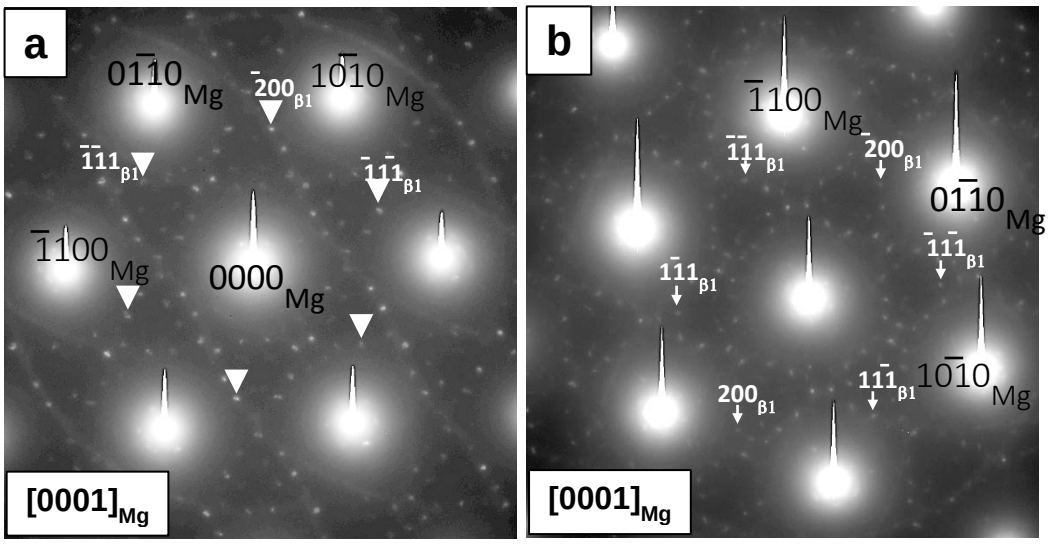

Figure 10 SAD pattern on [0001] zone axis (a) 100 hrs creep tested sample (b) 100 hrs annealed sample

After close examination of Figure 10a and 10b, very fine precipitates are visible near the β_1 precipitates. The streaking from these precipitates seems to be located at ½ {10-10} and ½ {11-20} in $[0001]_{Mg}$ SAD pattern (Figure 10a and 10b). Due to their very fine scale, the identification of these precipitates is difficult. Therefore, HAADF-STEM imaging was performed on isothermally annealed and creep tested condition to examine fine-scaled precipitates. All images were obtained along $[0001]_{Mg}$ axis (Figure 11). Fine scale precipitates are observed in the vicinity of fine scale precipitates in Figures 11a and 11b. The Figure 11b shows high density clusters of fine scale precipitate near the elongated precipitate. Figures 11c and 11d shows high magnification HAADF-STEM image revealing fine scale precipitates in the vicinity of elongated precipitates. The lenticular morphology of fine scale precipitates is evident from Figures 11c and 11d.

Saito reported precipitates with similar morphology i.e. β′ (orthorhombic, a=0.64 nm, b=1.14 nm, c= 0.52nm). The SAD pattern along $[0001]_{Mg}$ zone axis shown in Figure 12 confirms

β′ precipitate Figure 12. The reflections from precipitates observed at ½ {10-10} and ½ {11-20} in $[0001]_{Mg}$ SAD pattern of Figure 12 were indexed as β′ [5].

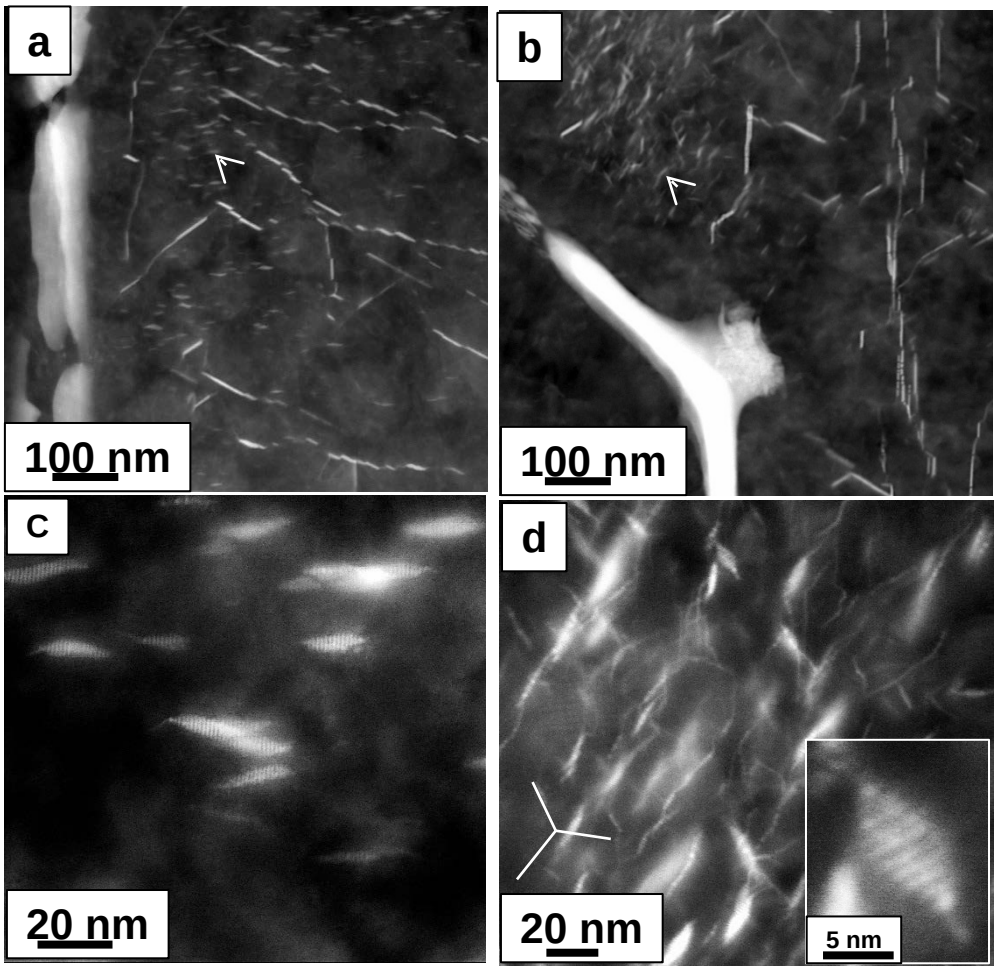

Figure 11 HAADF-STEM (a) 100 hrs creep tested sample (b) 100 hrs isothermally annealed sample (c) high magnification of HAADF-STEM 100 hrs creep tested sample (d) high magnification of HAADF-STEM 100 hrs isothermally annealed sample

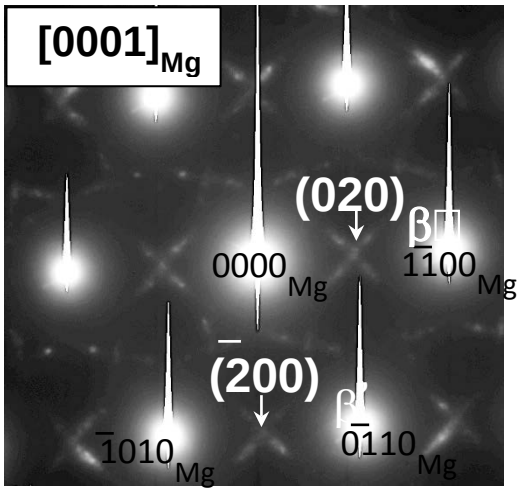

Figure 12 SAD of β′ precipitate of creep tested sample

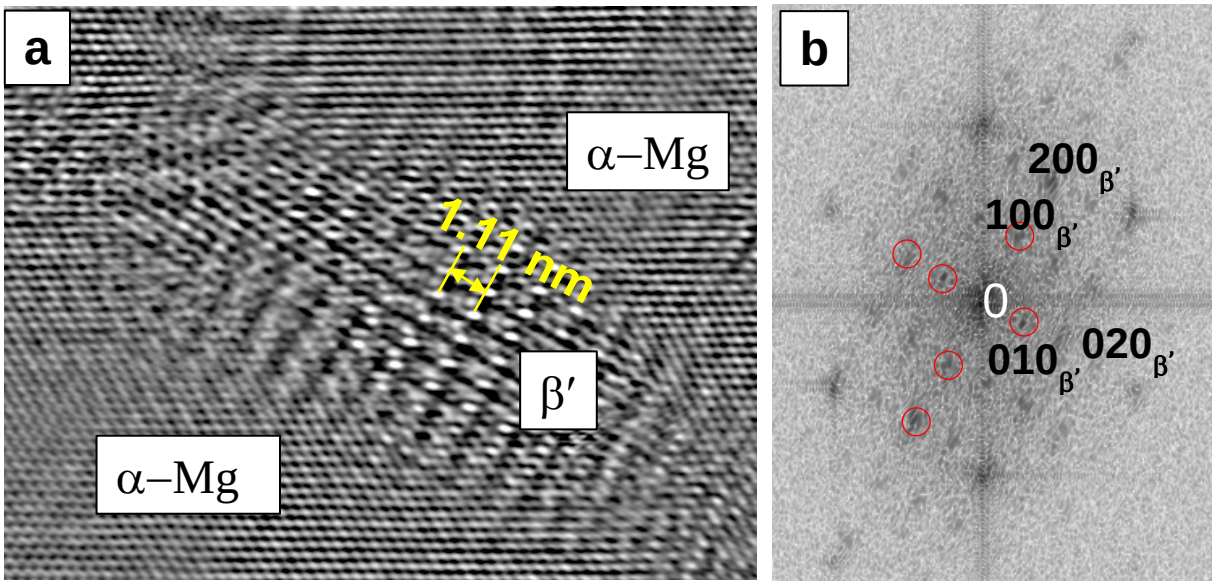

Figure 13 (a) HRTEM of 100 hrs from creep tested sample (b) FFT of β′

From these Figures, it appears that β′ precipitates grow and coarsen more rapidly in creep tested condition as compared to isothermally annealed condition. The precipitates of this size scale of β′ did not appear in the 5 hrs isothermally annealed condition. This indicates that formation of β′ must have occurred between 5 to 100 hrs isothermal annealing. For clear understanding of β′, HRTEM was carried out for isothermally annealed and creep tested

condition. An HRTEM image shown in Figure 13a showed that the precipitate of β′ is coherent with the α-Mg matrix. The corresponding FFT confirms the presence of orthorhombic structure of β′ (Figure 13b).

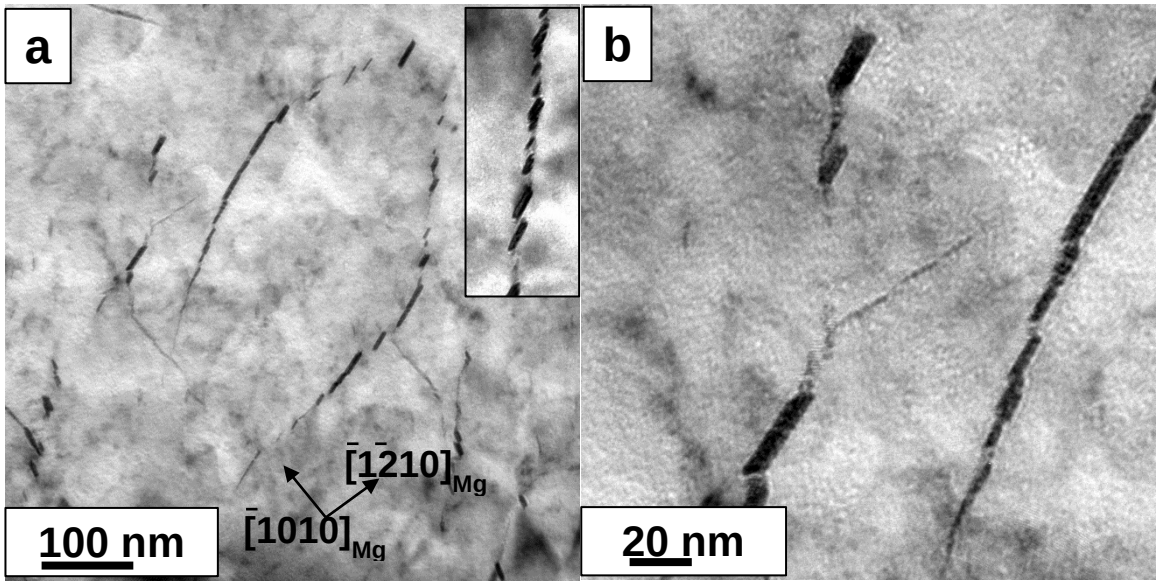

Figure 14 BF-TEM images (a) 100hrs creep tested sample (b) high magnification image of β_1 plates in 100 hrs creep tested sample

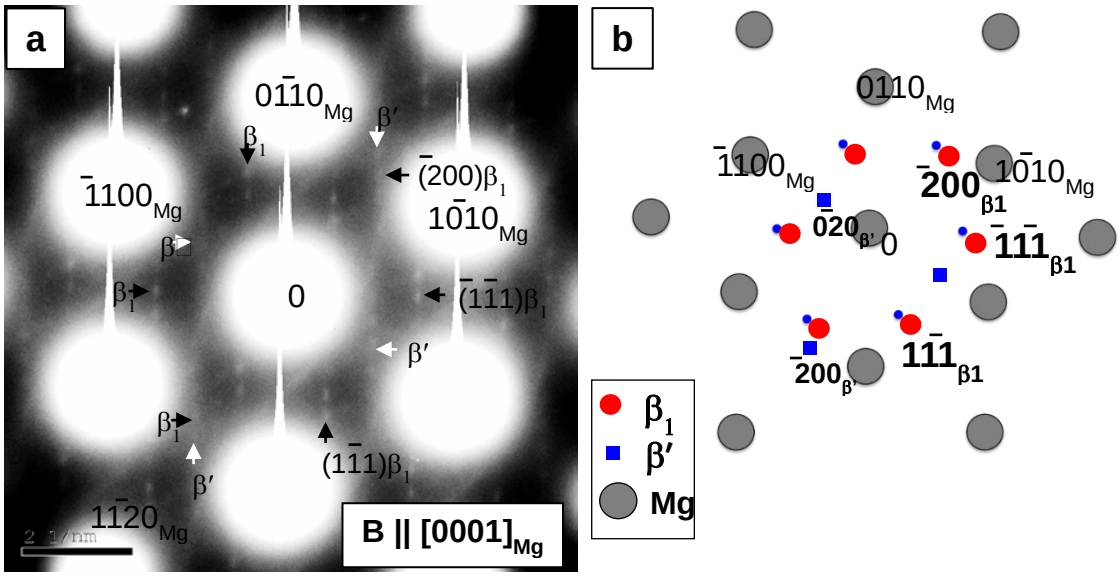

Figure 15 (a) SAD pattern on [0001] zone axis from 100 hrs creep tested sample (b) schematic representation of one variant of β′ & β1.

In the 100hrs isothermally annealed and creep tested conditions, the presence of β_1 precipitates were prominent throughout the sample. The Figure 14a and 14b showed BF-TEM images of creep tested condition respectively. A possible preferential alignment of β_1 precipitates was observed in the creep-tested condition along the loading direction (Figure 14b). The β_1 precipitates followed a curved or linear trajectory decorating dislocation lines. The SAD pattern along $[0001]_{Mg}$ axis was shown in Figure 15a. Some of reflections from precipitates observed (black arrow) in diffraction pattern were consistently indexed as β_1 (Fm-3m, a=0.74nm) [5]. The orientation relationship between β_1 and α-Mg matrix was determined to be $(110)_{\beta 1} \parallel (0001)_{Mg}$ & $[-11-1]_{\beta 1} \parallel [2-1-10]_{Mg}$ consistent with previous reports[5]. The remaining reflections were from β′. For clear understanding, the Figure 15b represent schematic diagram of one variant of β′ & β_1.

The Figure 16 shows BF-TEM image of 100 hrs isothermally annealed sample. The β_1 precipitates follow curved / linear trajectory which indicates β_1 precipitates forming on dislocation line. It observed that β_1 in isothermally annealed condition appear to have structural gap. This structural gap in β_1 precipitates was shown in Figure 16a. In contrary to this, structural gap in β_1 precipitates were absent in the creep tested sample (Figure 14b).The Figure 16b shows structural gap between β_1 plates. The Figure 16b shows high magnification image of β_1 plates with structural gap.

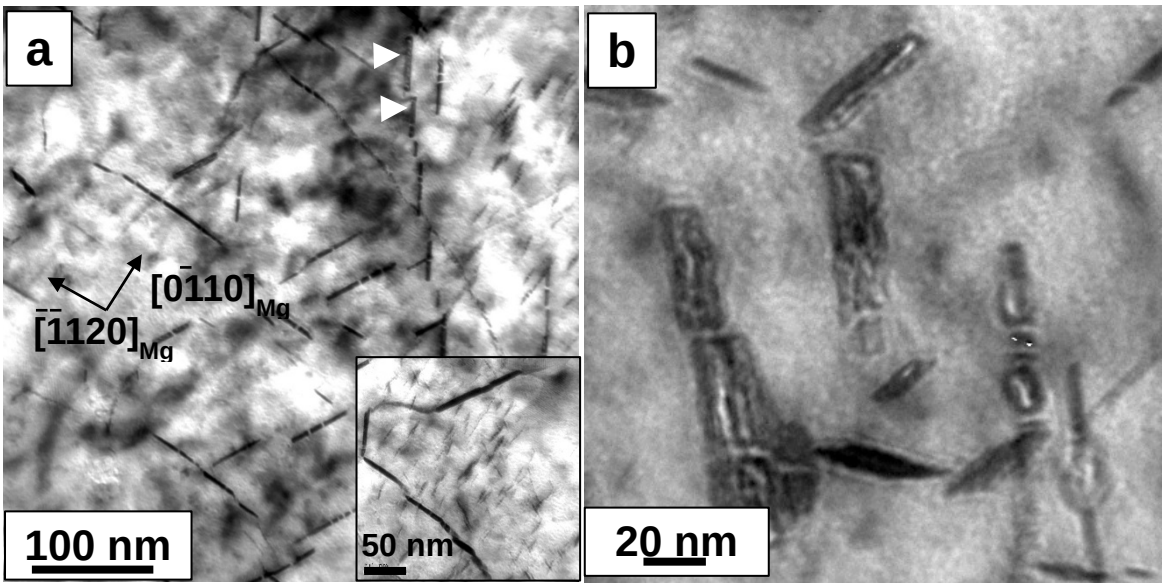

Figure 16 BF-TEM images (a) 100 hrs isothermally annealed sample (b) high magnification image of β_1 plates in 100 hrs isothermally annealed sample

Firstly, comparison of the BF images in Figures 5c and 5d indicate that the β_1 plates appear to largely lie preferentially on a specific set of $\{10\text{-}10\}_{Mg}$ planes $<11\text{-}20>_{Mg}$ directions in case of the sample subjected to creep, whereas the β_1 plates lie on more sets of $\{10\text{-}10\}_{Mg}$ planes $<11\text{-}20>_{Mg}$ directions in the isothermally annealed specimens. In both cases these β_1 plates appear to follow a trajectory (linear or curved) indicating that these precipitates are decorating dislocation lines in the matrix. These observations after 100 hrs creep/ annealing appear to follow a consistent trend progressing from the 5 hrs creep/ annealing condition.

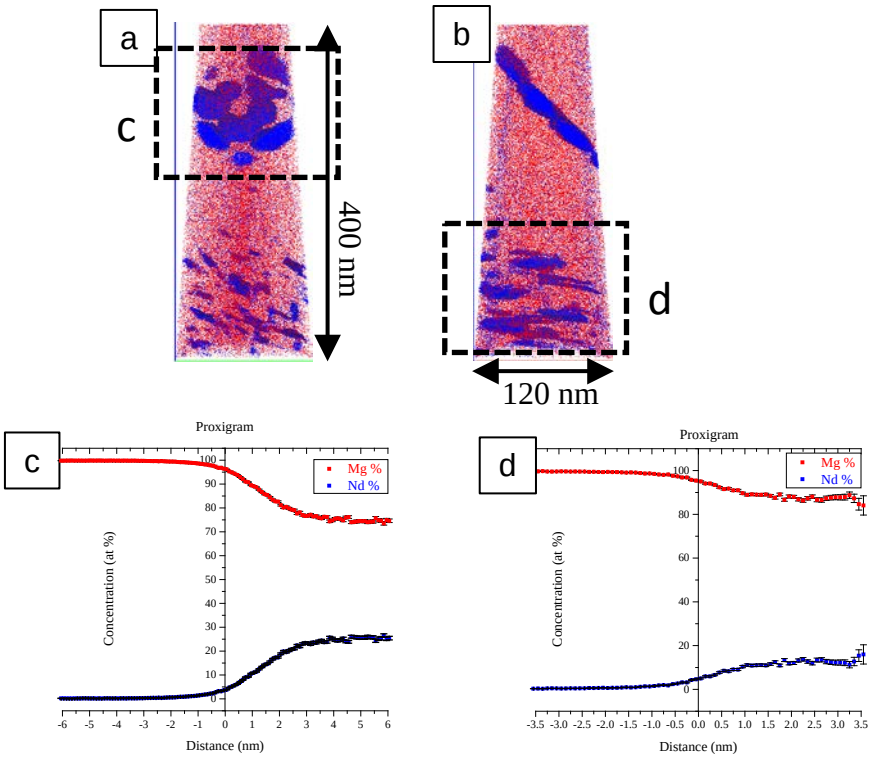

Figure 17 (a) 3D reconstruction marked with β_1 precipitates (b) 3D reconstruction marked with β' precipitates (c) proxigram of precipitates from dotted box c (d) proxigram of precipitates from dotted box

The Figure 17 shows the result of APT from the 100hrs-aged condition. The Figure 17a and 17b showed reconstruction containing β' and β_1 precipitates along two different views. The proxigram obtained for dotted box c containing precipitates showed ~25 at% Nd composition (Figure 17c). This composition of Nd ion matches with Mg_3Nd i.e. β_1. From Figure 17a and 17b, β_1 seem to be formed on network prior defects. The other proxigram for dotted box d containing precipitates showed composition of Nd ~12.5 at% which matches with Mg_7Nd i.e. β' (Figure 17d). The results obtained from APT supports the existence of β' & β_1 as observed in TEM results.

3.3.5. Late Stage Of Precipitation During Creep And Isothermal Annealing (~230 hrs)

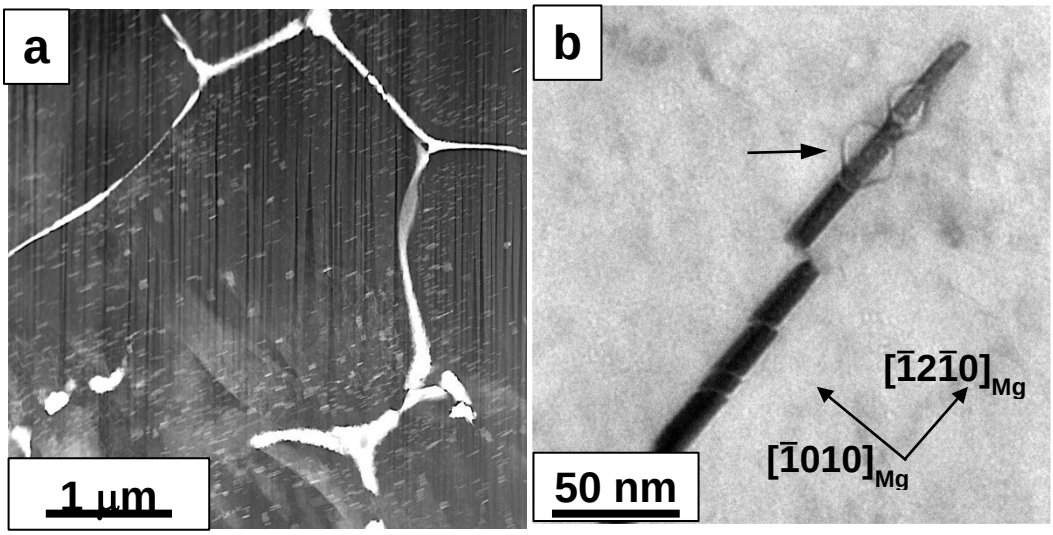

Figure 18 BF-TEM image (a) 230 hrs creep tested sample (b) high magnification image showing plate like precipitates.

The preferential arrangement of β_1 precipitates were observed in the creep tested to failure (Figure 18a). These β_1 precipitates were preferentially oriented only one direction $<11\text{-}20>_{Mg}$ direction. The Figure 18 b shows pinning of dislocation loops by the β_1 precipitates in the creep tested sample.

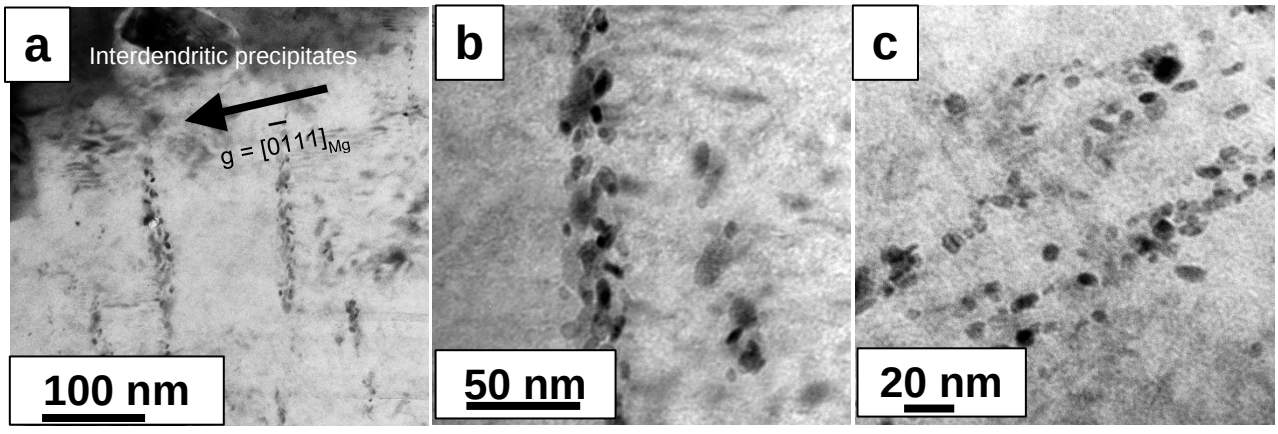

Figure 19 BF-TEM image (a) 230 hrs isothermally annealed sample (b) high magnification image showing bands of globular precipitate (c) high magnification image showing bands of globular precipitate

The bands of globular precipitates were observed in 230 hrs isothermally annealed sample in Figure 19a to 19c. It appears that these globular precipitates were formed near the prior β_1 precipitates. The structural gap in β_1 precipitates of 100hrs aged sample (Figure 16b) may have transform to the globular precipitate after 230 hrs ageing (Figure 19).

3.4. Discussion

From experimental results, it is clear that the applied stress during creep testing has significant impact on precipitation of β_1 and β'precipitates in Mg-Nd alloys.

1. The β'precipitates are expected to be coherent (Figure 6a and 13a). According to Nie and Muddle, β_1 precipitates are incoherent. The interfacial energy between β' and α-matrix is expected to be lower than the β_1 and α-matrix. Therefore, activation energy required to form β'precipitates is much lower than the β_1 precipitates. This permits homogeneous nucleation of β' precipitates. The external stress during creep testing accelerates homogeneous nucleation and growth of β' precipitates throughout the α-matrix.
2. The β_1 precipitates are incoherent. Therefore, the activation energy required to form this precipitate is higher than β' precipitate. In order to nucleate this precipitate, high energy sites such as dislocation, vacancy, etc. in the α-matrix are required. Hence, β_1 precipitates preferentially form on dislocation lines present in the α-matrix of both creep tested and isothermally annealed condition. It is clear that growth of homogeneously distributed β' precipitates throughout the matrix in creep tested condition is faster than isothermally annealed sample for similar time frames of exposure at the same temperature. The β_1 precipitates prefer to nucleate and grow on dislocation lines within the Mg-Nd matrix. Due to faster growth of the homogenously distributed β' precipitates, the super-saturation of Nd in the α-matrix is depleted which leads to slower growth of β_1 precipitates. In case of

isothermally annealed sample, the β_1 precipitates decorating the dislocation line grow and thicken rapidly due to slower rate of nucleation and growth of the β′ precipitates.

3.5. Conclusion

Based on the results and discussion from above experiments, following conclusion are drawn

1. Early stage of creep and isothermal annealing

   In isothermally annealed sample, localized Nd enriched regions were observed. The β′ precipitates seem to be homogeneously distributed throughout the α-Mg matrix in the creep tested condition. The applied stress promotes the formation of β′ precipitates presumably by reduction of activation barrier for β′ nucleation as well as stress assisted accelerated diffusion of Nd atoms.

2. The β_1 precipitates decorating the dislocation lines were observed in both creep tested and isothermally annealed condition (after 5hrs, 100hrs and 230hrs exposure). The coarser β_1 precipitates were observed in isothermally annealed sample compared to creep sample. After 5 hrs isothermal annealing, the slower nucleation and growth of β′ precipitates in the α-matrix as compared to creep tested sample led to a higher degree of supersaturated Nd solutes retained within the α-matrix which facilitates the faster growth and coarsening of β_1 precipitates. On other hand, rapid rate of nucleation and growth of β′ precipitates in creep tested sample depletes Nd content in the α-matrix which inhibits coarsening of β_1 precipitates.

CHAPTER 4

CHARACTERIZATION OF FINE-SCALE PRECIPITATE IN THE HOT ROLLED AND AGED WE43 ALLOY

4.1. Introduction And Motivation

Precipitation hardenable WE43 (of Mg-Y-Nd family) consist of metastable β'' (DO_{19}), β' (bco), β_1(fcc) and equilibrium β (fcc) precipitates in α-Mg matrix [7, 17, 22-26]. According to previous studies, it has been found that β'', β_1 and β precipitates show a plate-like morphology and β' shows a globular morphology [7, 17, 22-26].

Earlier studies, the characterization of above mentioned precipitates had been carried out in as-cast, solutionized, and aged alloys [1-5]. However, as cast and solutionized alloys are often exposed to hot rolling prior to ageing for industrial application (e.g. T5 or T6 treatments). Therefore, a complex dynamic precipitation process takes place in the α-Mg matrix due to hot deformation [3, 27-29]. Furthermore, precipitate evolution may be affected due to stresses generated during hot rolling [28].

The aim of this study is to investigate the precipitation in WE43 just after hot-rolling and subsequent aging. This study has been carried out using APT, SEM and TEM

4.2. Experimental Procedure

The nominal composition of WE43 alloy is as follow Mg- 3.7-4.3 wt% Y, 2.4-4.4 wt% RE, and 0.5wt % Zr. As cast WE43 alloy was solutionized at 525°C for 8 hrs. After solutionizing treatment, this material was hot rolled to 95% reduction in thickness. This hot rolled material subsequently subjected to ageing at 210°C for 48 hrs. All above-mentioned processing were

carried out at Magnesium Elektron Ltd. The microstructural analysis was carried out using SEM (FEI Nova-NanoSEM 230) and TEM (TECHNIAI-TF20 microscopes). The atom probe study (LEAP 3000XHR, Cameca Inc.) was done to measure composition of precipitates. The focused ion beam (FIB) was used to prepare site-specific atom probe samples. The further processing of these samples was carried out as mention in chapter 2.

4.3. Results

4.3.1. Hot rolled condition

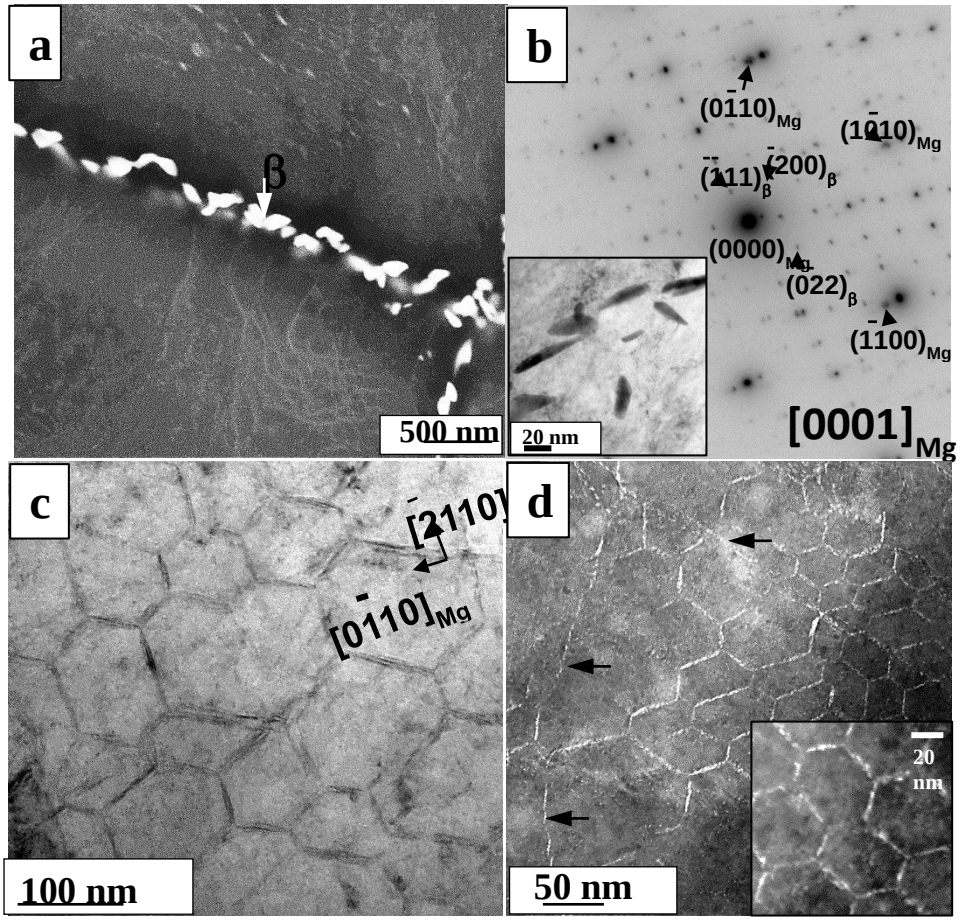

Figure 20 (a) Microstructure of hot rolled sample (b) SAD pattern of β precipitate (c) BF-TEM image showing orientation and habit plane of individual arm of honeycomb like precipitate (d) HAADF-STEM showing partitioning of heavy elements.

The microstructure of hot rolled samples showed very fine intra-granular precipitates in some cases forming network and coarser precipitates at the grain boundaries (Figure 20a). The Figure 20b shows SAD pattern obtained from coarser precipitates were indexed as equilibrium β along [0001] zone axis. The morphology of β phase appears elongated in nature. The length of this precipitate found to be ~200 nm to 500 nm. From the microstructure of hot rolled sample, it observed that β precipitates seems to be formed on either grain boundaries or twin boundaries. The networks of very fine precipitate were found near the grain or twin boundaries. Therefore, TEM study was carried out for details investigation of fine-scaled precipitates.

The Figure 20c shows BF-TEM image of honeycomb network of fine-scaled precipitates. The individual arms of honeycomb structure lie on $\{10\text{-}10\}_{Mg}$ planes. Due to low volume fractions of very fine-scaled honeycomb network of precipitates, the precipitate reflections in $[0001]_{Mg}$ were absent. The honeycomb arrangements of precipitates were shown in a HAADF-STEM image (Figure 20d). The HAADF-STEM image (Figure 20d) shows clearer picture of honeycomb network and fine vein type of structure (marked by arrow). The bright region in HAADF-STEM image indicated that the heavier elements were partitioned in that region. The APT study was carried out in order to probe 3D morphology of precipitates and their composition.

Table 2 Listing of bulk and precipitate composition in at. % measured with atom probe

Ions	Hot rolled		Aged		
	Bulk composition (%)	Honeycomb Network	Bulk composition (%)	Honeycomb Network	
				β_1	β'
Mg	96.23	82.2	96.41	79.6	83.2
Nd	0.40	9.6	0.48	16.0	3.0
Y	0.59	1.7	0.70	1.5	4.9
Ze	0.46	2.0	0.43	2.9	7.3
Impurities (Dy, Gd, Al, Si)	1.17	1.6	1.14	2.9	1.6

Figure 21 shows APT results of hot rolled samples. Figure 21a shows 3D reconstruction of precipitates in α-Mg matrix. These precipitates were revealed using 2 at% Nd iso-surface. The interconnected networks of precipitates were shown in Figure 21a. The dotted boxes b and c marked on precipitates in reconstruction were shown in Figure 21a. Figure 20b and 21c showed view from orthogonal direction parallel to axis of reconstruction. Figure 21b showed interconnected network of precipitates. The honeycombs like arrangement of precipitates were shown Figure 21c. From Figures 21a to 21c, it is observed that morphology of precipitate appear to be plate shaped in honeycomb structure of precipitates.

The proxigram shows plot of concentration versus distance. Figure 21d showed proxigram of precipitates observed in Figure 21a indicating partitioning of Y, Nd and Zr across precipitate/α-Mg interface. The Figure 21d shows greater partitioning of Nd (~9.6 at %) into

precipitates compared with Zr (~2 at %) & Y (~1.7 at %). These fine-scaled precipitations appear to be in early stage of precipitation. Therefore, composition of precipitates was compared with β″ formed in early stage of precipitation during ageing of WE43 or WE54 alloy [17, 20]. The ratio of Mg/(Nd+Y+Zr) was compared to previously reported β″ of aged alloy (Table 2 and Table 3). Though, these ratios are quite different.

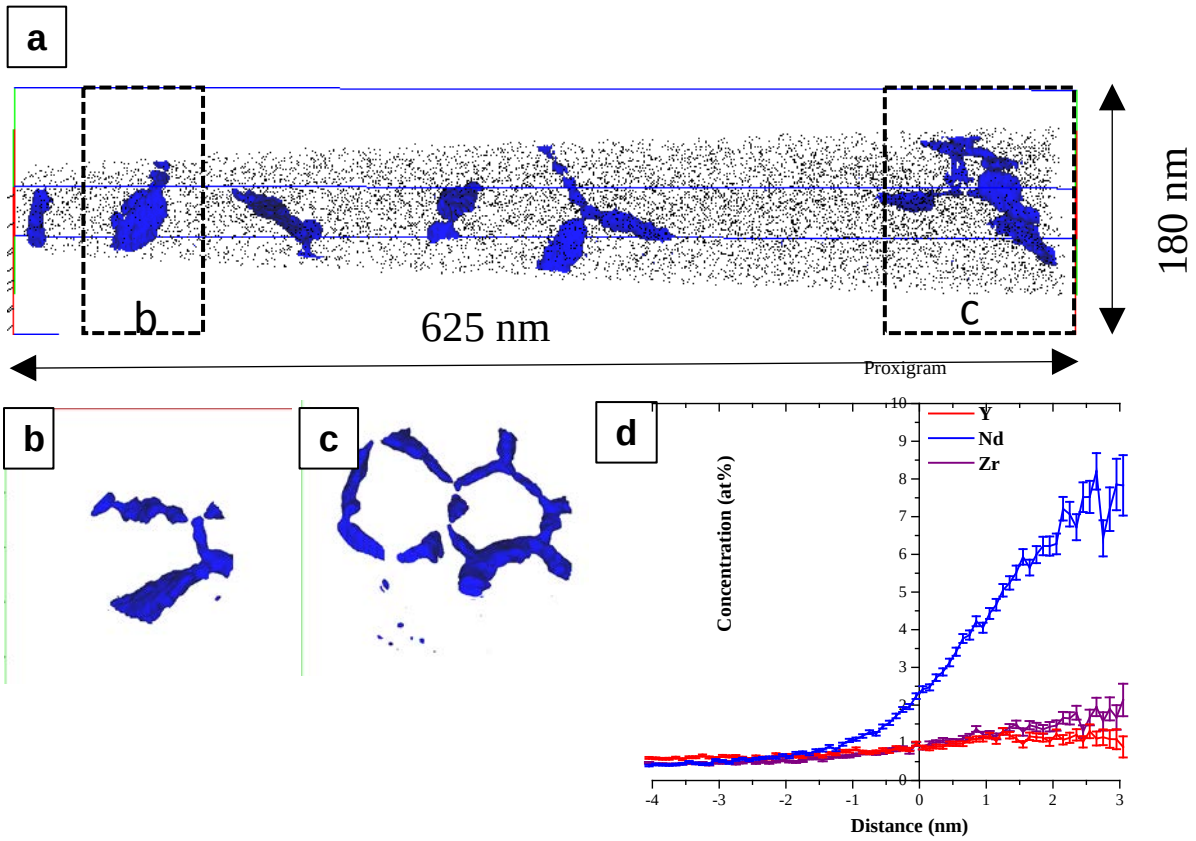

Figure 21 (a) 3D reconstruction of interconnected precipitate in hot rolled sample (b) clipped part of interconnected precipitate (c) clipped part of honeycomb like precipitate (d) proxigram of interconnected precipitate

Table 3. Ratio of Mg/(Nd+Y+Zr+impurity) obtained from APT results. Mg/(Nd+Y) ratio of β′ and β_1 in Mg-Nd alloy, while ratio of β″ is 3

Honeycomb network precipitate		
Hot rolled	Aged-β_1	Aged-β′
6	3[3]	5[6]

4.3.2. Aged condition

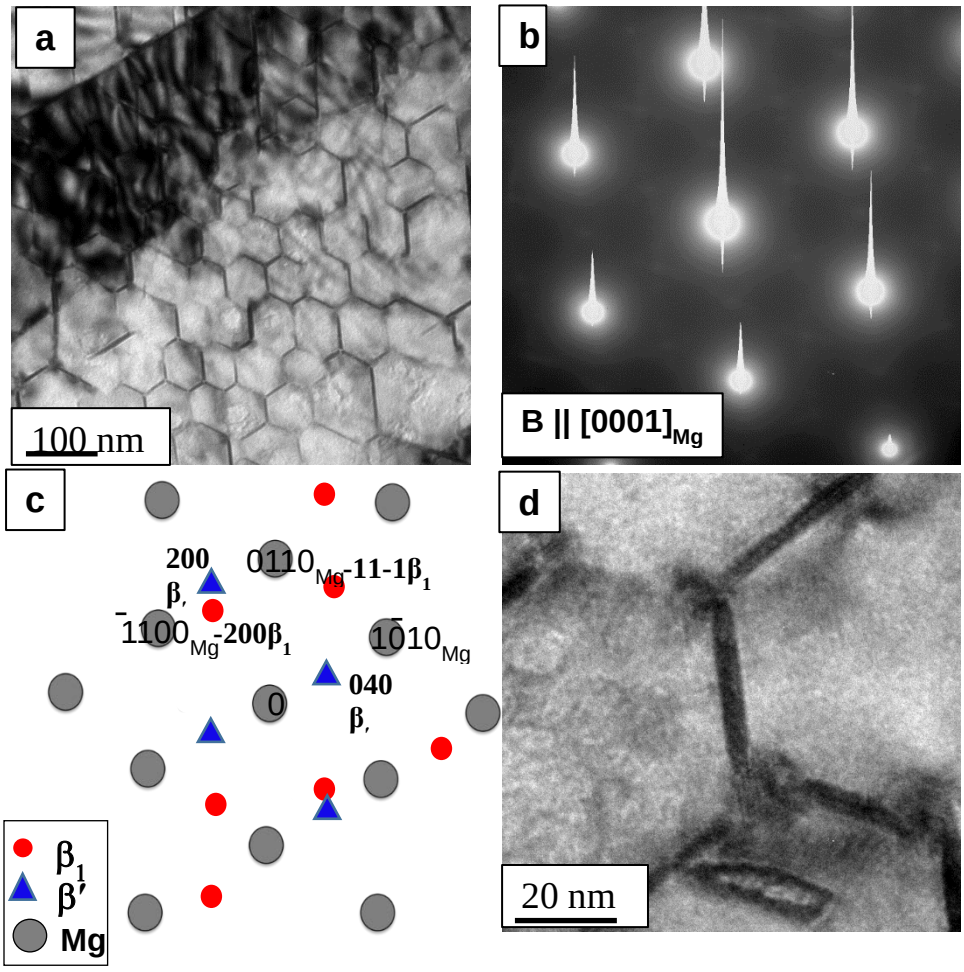

Figure 22 (a) BF-TEM image of honeycomb precipitate (b) SAD pattern of honeycomb precipitate (c) schematic diagram showing one variant of β_1 & β′ (d) BF-TEM of β_1 & β′

Figure 22a shows a BF-TEM image of precipitates with honeycomb arrangement in aged sample. Similar to hot rolled sample, an individual arm of honeycomb arranged precipitates lied

in $\{10\text{-}10\}_{Mg}$ plane and oriented along <11-20> directions. It was observed that the growth and coarsening of precipitates in honeycomb network were observed in Figure 22a. Figure 22b shows SAD pattern along [0001] zone axis on honeycomb network of precipitates. The reflections from precipitates were observed as cross pattern (X) at the ½ $\{10\text{-}10\}_{Mg}$ and ½ $\{11\text{-}20\}_{Mg}$ locations. The bright spots were found at ½ {10-10} and ½ {11-20} and faint spot was located at extremities of the X pattern. This suggested the presence of two type precipitate. Thus, SAD pattern was indexed based on presence of two types of precipitates i.e. β′ & β_1 Figure 22c. The β′ phase has body centered orthorhombic crystal structure (a=0.64 nm, b=2.24 nm, c= 0.52 nm) and β_1 has fcc structure (a=0.735 nm). Figure 22d shows BF TEM of β′ & β_1 precipitates. The β′ precipitates showed oval shaped morphology. The multiple variant of β_1 precipitates were connected to β′. This observation matches with previously reported by Nie and Muddle in case of WE43 alloy [17, 20].

Figure 23 shows APT results obtained from aged sample. The reconstruction in Figure 23a shows the interconnected network of precipitates. The Y ion & Nd ion are indicated by red and blue colors respectively. The Nd rich plates were connecting to Y rich oval shaped precipitates in the reconstruction shown in Figure 23a. The isosurfaces with 4.2 at % Nd and 3.1 at % Y were used to segregate Nd and Y rich precipitate as shown in Figure 23b& 23c respectively. These isosurfaces clearly shows Nd rich plates connected via Y rich oval shaped precipitates. This network of precipitates consistently matches with TEM results. The proxigram corresponds to 4.2 at % Nd and 3.1 at % Y isosurfaces were plotted and shown in Figure 23d and 23e respectively. The composition of plate and oval shaped precipitates were listed in Table 2. The ratio of Mg/(Nd+Y+Zr) was compared to previously reported ratio in WE43 or WE54 alloy. These ratios show that plate shaped precipitate is β_1 and oval precipitate is β′.

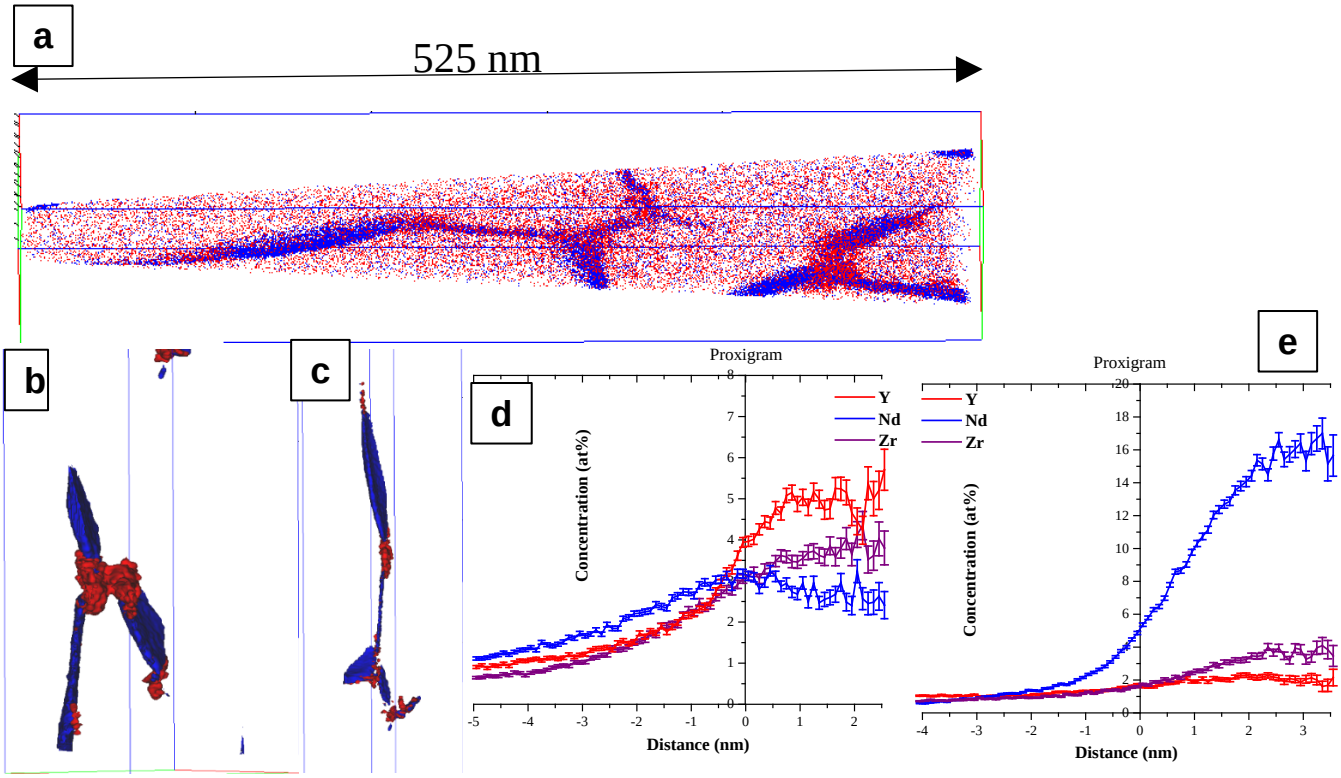

Figure 23 (a) 3D reconstruction of honeycomb network precipitate in aged sample (b) clipped part of 4.2 at % Nd iso-surface (c) clipped part of 3.1 at % Y iso-surface (d) proxigram showing β_1 (e) proxigram showing β'

4.4. Discussion

The processes such as plastic deformation, dynamic recovery and dynamic precipitation take place during hot rolling of magnesium alloy [3, 27-29]. During recovery, the rearrangement of dislocation generated from plastic deformation leads to subgrain boundary formation [3, 27-29]. It is observed that the vein like precipitates (Figure 20a and 20d) may have formed on the subgrain boundaries

It is observed that in the twist boundaries in pure Al (fcc), dislocations can arrange themselves in hexagonal networks on the close packed $\{111\}_{Al}$ planes[30]. Similarly, the arrangement of dislocations in hexagonal network on close packed plane i.e. {0001} can take

place during hot rolling of WE43 alloy. From results, it is seen that honeycomb like network of Nd rich precipitates observed in hot rolled sample (Figure 20 and 21) which are precursors to the formation of well-developed honeycomb precipitates (Figure 22 and 23). In case of hot rolling, the diffusion of Nd solute atoms takes place by short circuit diffusion. The Nd diffusion decorates the dislocation networks which lead to formation of the honeycomb like precipitates (Figure 20 and 21). On further ageing, the well-developed precipitates formed coarsening via thickening of precipitates. After ageing, the preferential partitioning of Nd atoms took place into plate shaped precipitates, while other elements remain constant (table 2).

The above-mentioned results suggested that β′ precipitates were observed only in aged sample which were not seen in the hot rolled samples. The β_1 precipitates were clearly seen in the hot rolled as well as aged samples. Nie reported that β_1 precipitates have a tendency to nucleate on dislocations [26]. Due to presence of prior defects, precipitation sequence may have influenced.

4.5. Conclusion

Based on above mentioned results and discussion, following conclusions are drawn.

The honeycombs like network of precipitates were formed in hot rolled sample. These structures seem to be formed on dislocation subgrain boundary formed during dynamic recovery process. The individual arms of honeycomb precipitated were lying in $\{10\text{-}10\}_{Mg}$ planes. These precipitates seem to be precursors to the precipitates, which formed on further ageing.

The well-developed honeycombs shaped precipitates were formed on ageing of hot rolled specimen. The multiple variants of plates shaped precipitates were connected via oval shaped

precipitate. Based on APT & TEM analysis, Nd rich plate shaped precipitate is β_1 and Y rich globular precipitate is β'.

CHAPTER 5

EVOLUTION OF MICRO-TEXTURE IN THE FRICTION STIR PROCESSED (FSP) REGION OF MG-Y-RE ALLOY

5.1. Introduction And Motivation

Magnesium alloy is one of the lightest metals in use for structural applications. These alloys have poor formability due to the limited slip systems in the hexagonal close-packed (hcp) structure of magnesium, which imposes manufacturing limitations [31, 32].

As per previous study, the formability of magnesium alloys had improved by modifying the texture of alloy [33]. The randomization or weakening of texture in materials improves formability properties. The commercial WE43 alloy is composed of high content of RE and Yttrium. The weakening or randomization of texture observed in the WE54 alloy after hot deformation [34]. The weakening of texture is caused due to presence of RE or Y element in the alloy. The recrystallization mechanism of this alloy was influenced by these elements. It had been found that the main mechanisms for weakening of the texture are particle-stimulated nucleation (PSN) during recrystallization and solute drag effect. The weakening of texture caused due to PSN effect was observed in the hot extruded WE43 alloy [34, 35]. However, this mechanism does not appear to dominate the final texture.

Mackenzie et al. [34] explained that there are mechanisms other than PSN to develop the final texture i.e. solute drag or particle pinning. In the solute drag or particle pinning, the RE elements in the WE43 alloy influence high boundary mobility. This change in boundary mobility leads to produce non-basal texture. It has been observed that there is growth of grains with non-basal oriented grains over basal oriented grains [36, 37].

In order to improve formability of Mg alloys, friction stir processing is widely used to modify the texture by refining microstructure. It is challenging to predict material flow during friction stir processing. Several studies have been done to analyze material flow. Park et al [38] explained that the existence of ellipsoidal basal texture during FSW causes formation of the nugget shape and O-ring structure in stir zone. They suggested that basal plane is roughly aligned parallel with tool pin surface in the friction stir zone. The local micro-texture components in a weld of 6063 Al were studied [39]. They demonstrated that dynamic recrystallization during FSW leads to formation of weld center. Field reported that dominance of 70° rotation from the normal to the axis of weld tool outward radially of texture component is kind of mysterious [40].

The aim of this work is to study the effect of ageing on micro-texture evolution in FSP region of WE43. This work give difference between micro-texture evolutions in processed FSP and aged FSP.

5.2. Experimental Procedure

A 5.25 mm thick hot rolled plates of WE43 alloy with a nominal composition Mg – (4.0) Y – (3.3) RE – (0.5) Zr (wt. %) are supplied by Magnesium Electron North America, Inc. The WE43 alloy in cast condition is solutionized at 525^0C for 8 hrs and quenched in water. After solutionized treatment, WE43 alloy are hot rolled upto 95% thickness reduction at Magnesium Electron North America, Inc. Then, the friction stir processing was performed on these hot rolled plates as shown in Figure 24. The direction of the friction stir processing was perpendicular to the rolling direction of the plates. The parameters of the friction stir processing are 500 rpm (8.3 rev/s) tool rotation rate and 4 ipm (1.7 mm/s) tool transverse speed. The tool was made of tool steel. The diameter of tool shoulder was 12 mm. The geometry of the pin was in the form of truncated cone. The diameter at the pin intersection and the pin tip are 6.0 mm and 3.75 mm

respectively. The height of the pin was 2.2 mm. The specimen of 10 mm × 5 mm × 5.25 mm size was cut from the friction stir processed plates using electric discharge machining.

The scanning electron microscopy (FEI Nano Nova 230) was carried out for microstructural investigation and orientation mapping (electron backscattered diffraction). The cross section of the specimen was ground mechanically subsequently upto 1200 grit SiC paper and polished using alumina powder with 1 μm, 0.3 μm and 0.05 μm. The specimen was electropolished with in a solution of 40% Ortho-phosphoric acid + 60% ethanol using voltage of 20V for 10-15s at -15^0C. The site-specific platinum was deposited in the dual beam SEM (FEI Nova 200) at the horizontal centerline of the FSP region (Figure 25). The platinum deposits were separated from each other by a distance of 600 μm. The middle sites were identified as M. The distance 'n' mm from middle of friction stir zone was labeled as 'Mn' region. The negative sign with label correspond to retreating side and positive sign correspond to advancing side. The Pole Figures were obtained from sites corresponding to platinum deposits. The specimen was tilted at an angle of 70^0 to record orientation imaging microscopy (OIM) data. The accelerating voltage and corresponding current in the SEM for orientation mapping was set at 20kV and 6.1mA respectively. The scan step size for orientation mapping was maintained between 0.5 μm -0.7 μm. The reference directions for OIM are used as shown in fig 26. The recorded data are analyzed in the TSL software. An ageing was carried on the same specimen at 210^0C for 48 hrs. After ageing, this specimen was characterized using the same methods as mentioned above.

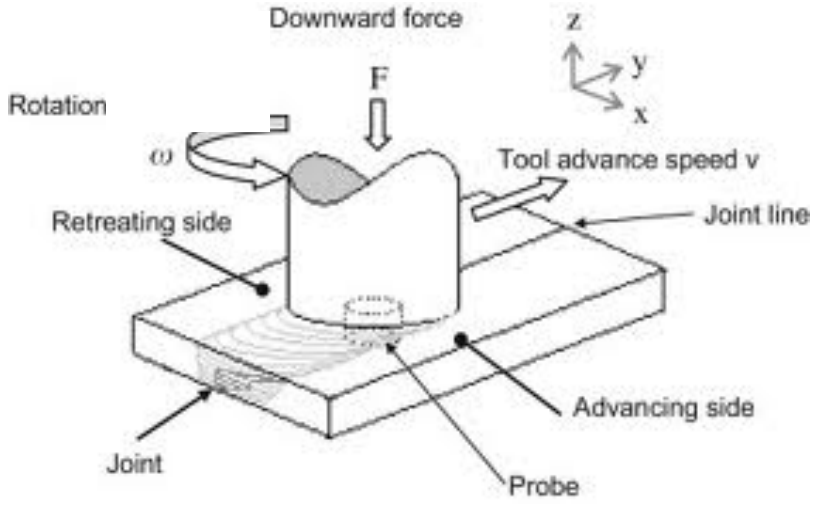

Figure 24 Schematic diagram of friction stir processing

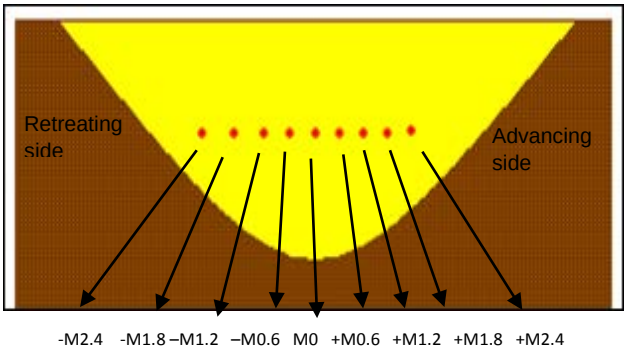

Figure 25 Platinum deposited site location for EBSD scan

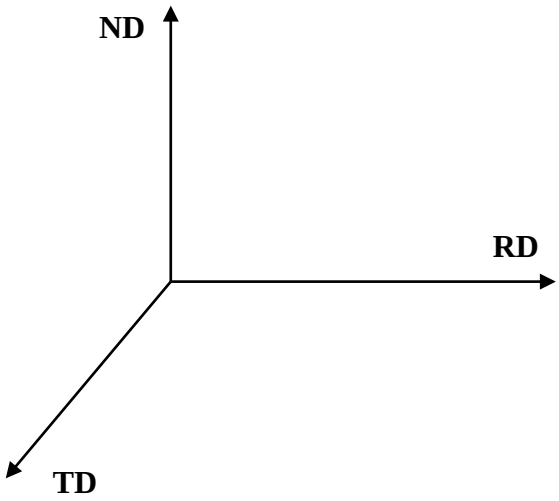

Figure 26 Reference axes corresponding to cross section of sample

5.3. Result

5.3.1. Microstructure

The microstructures of the hot rolled base material (BM), hot rolled FSP, hot rolled aged (aged BM) and FSP aged were obtained (Fig 27 a to d) by the backscattered electrons SEM imaging. The microstructure of hot rolled BM (Figure 27a) shows presence of high volume fraction of precipitates along the grain boundaries and twins. The high-volume fraction of precipitates are also observed in the hot rolled aged BM along the grain boundaries and twins as shown in Figure27b), but it is lesser than hot rolled BM. The grain sizes of hot rolled BM and hot rolled aged BM seemed to be comparable. The lesser volume fraction of precipitates observed in the hot rolled FSP region is mostly formed at the triple junction of grain boundaries (Figure 27c). As seen in Figure (27d), the higher densities of precipitates are found at the grain boundaries as well as inside the grains. The grain boundary precipitates seem to be discontinuous precipitates along the grain boundaries. However, the friction stirs zone shows equiaxed grain microstructure before and after ageing (fig 27c & 27d). After aging, there is no significant

difference in the grain size (fig 28). The high-volume fraction of precipitations at the grain boundary apparently retarded the growth of grain size in the aged FSP (fig 27d).

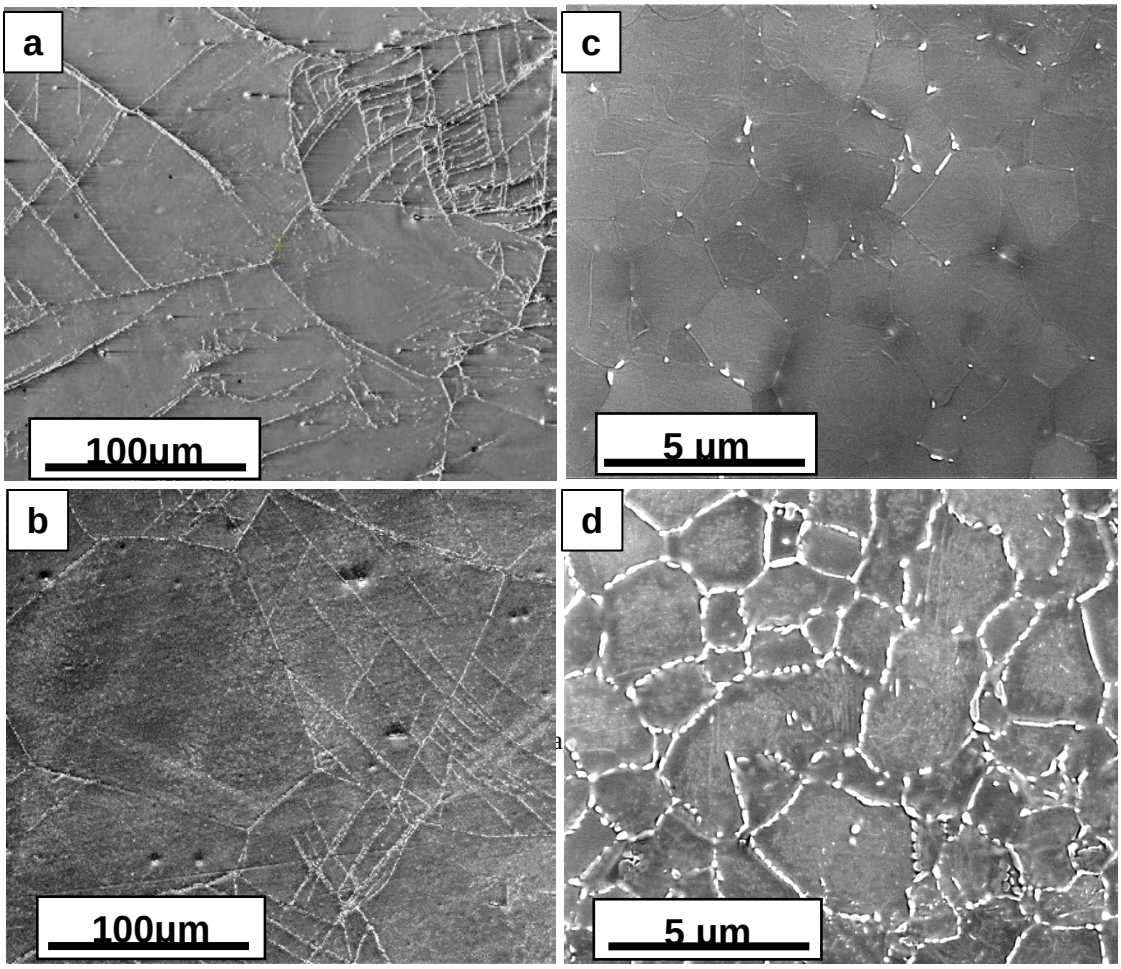

Figure 27 Microstructure (a) hot rolled BM (b) aged BM (c) hot rolled FSP (d) aged FSP

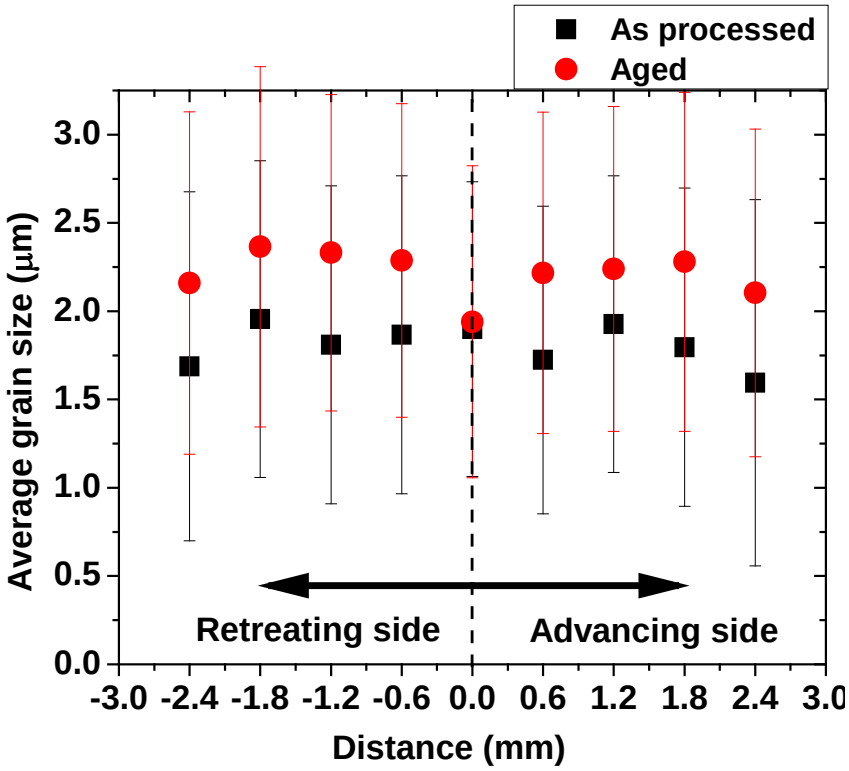

Figure 28 Plot of grain size vs distance in FSP region

5.3.2. Inverse Pole Figure (IPF) Map And Pole Figure Of Base Material

The orientation map of the hot rolled base material indicates large number of twins as shown in Figure 29 (a). The orientation of each grain can be correlated with inverse pole Figure map as shown in Figure 29 (e). The aged base material shows very less amount of twins as well as slight change in the grain orientation (fig 29 b). This change in the colors of grains in IPF indicates change in orientation. There is no significant difference between grain size of hot rolled BM and aged BM. Based on orientation mapping; the pole Figure of (0002) plane is plotted using OIM. As seen in Figure 29 (c), the basal planes of BM are aligned parallel to rolled surface along the normal direction. There is slight splitting in the basal plane orientation. After aging, the basal planes of base material showed more splitting than hot rolled BM. This splitting occurred

along the rolling direction (RD) as shown in Figure 28 (d). There is no significant change in the texture intensity.

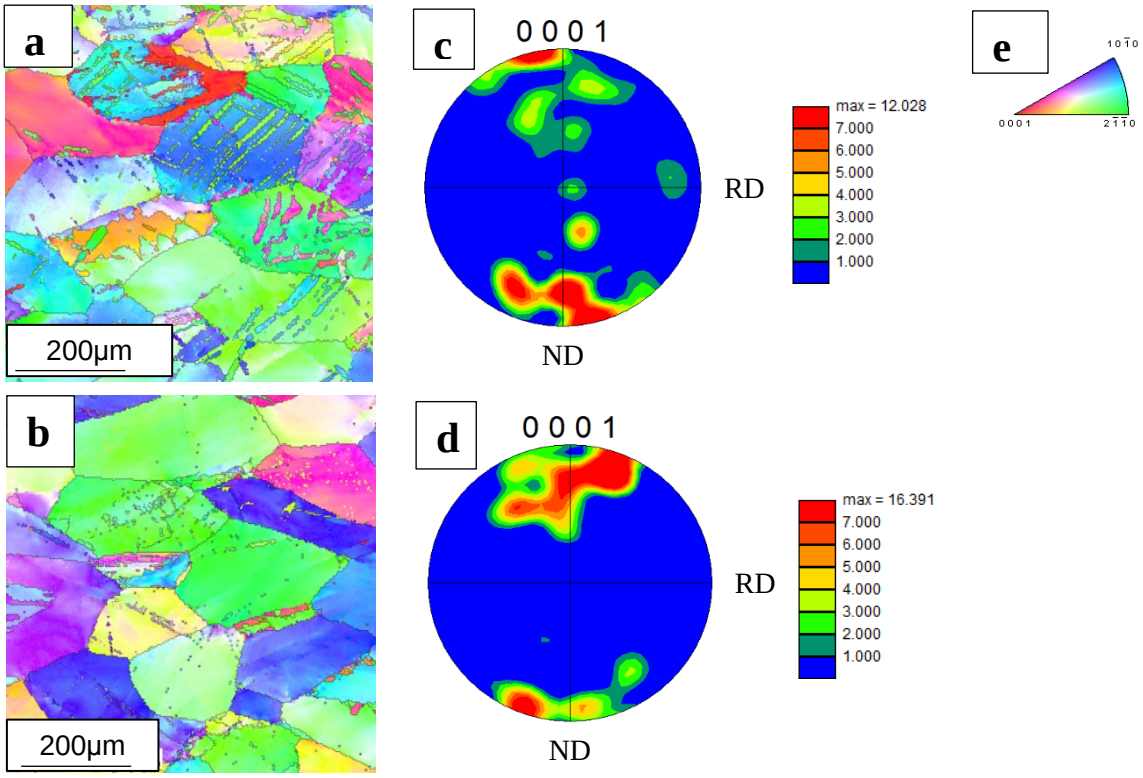

Figure 29 (a) IPF map of Hot rolled BM (b) IPF map of aged BM (c) pole Figure (0001) of hot rolled BM (d) pole Figure (0001) of aged BM (e) IPF map

5.3.3. IPF Map And Pole Figure Of Middle Of FSP

After friction stir processing of the hot rolled BM, the grain size became very fine. At low magnification, it is difficult to see the twin inside the FSP region Figure 30(a). The majority of grains of hot rolled FSP are oriented between {10-10} and {11-20} planes. After ageing, there are more grains having orientation of closer to {10-10} and {11-20} planes seen in Figure 30(b). The (0002) pole of the hot rolled FSP showed that the basal planes are oriented approximately 72^0 off the center toward normal direction seen in Figure 30(c). The significant amount of change in the orientation of grains in hot rolled FSP is occurred. The FSP leads to randomization

of texture. The same FSP region after ageing shows migration of basal plane toward RD seen in Figure 30(d). The texture of basal pole after ageing appears to become parallel to rolled surface.

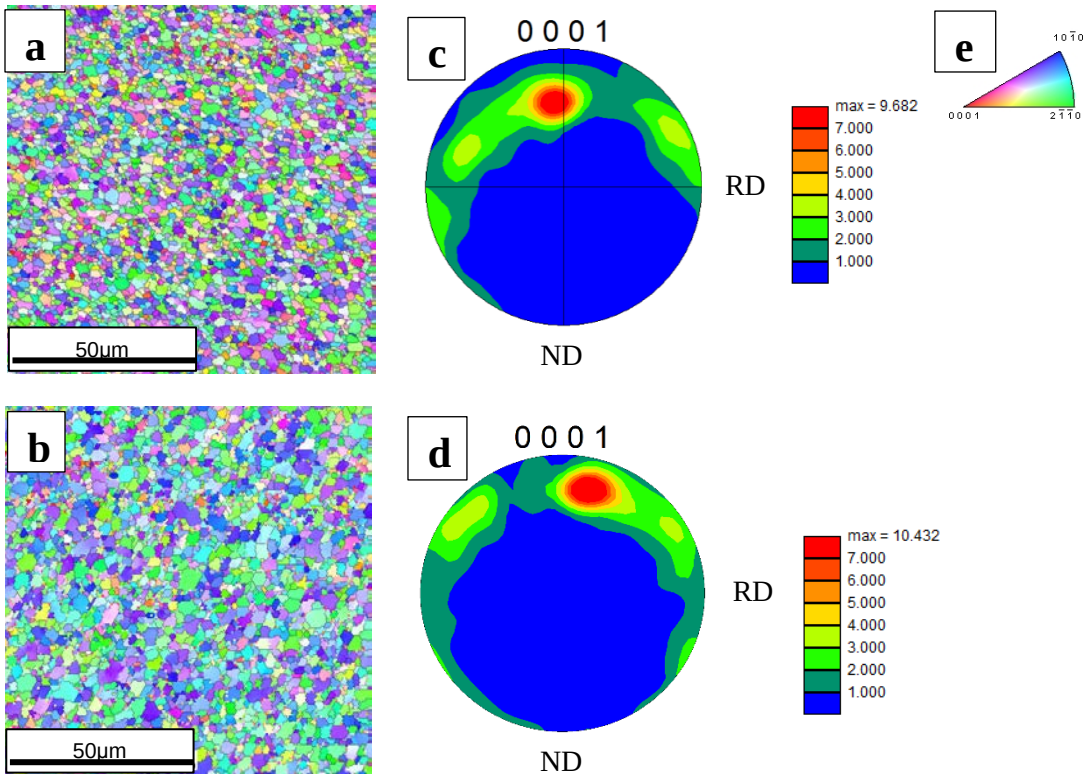

Figure 30 IPF map of Hot rolled FSP (b) IPF map of aged FSP (c) pole Figure (0001) of hot rolled FSP (d) pole Figure (0001) of aged FSP (e) IPF map

5.3.4. IPF Map Of Retreating Side

On the both side of FSP, there is significant change in the orientation of grains before and after ageing. As seen in Figure 31c & 31d for hot rolled FSP, an IPF map at –M1.2 and –M0.6 on the retreating side showed more grains with orientation closer to {10-10} & {11-20}. The same types of orientation of grains after ageing are observed at same location i.e. at –M1.2 and –M0.6 fig 31 (g & h). The IPF map at –M2.4 & –M1.8 in hot rolled FSP showed significant change in the orientation of grains Figure 31 (a, b) respectively. There is increase in the grains with orientation closer to (0002) and decrease in the grains with orientation {10-10} & {11-20}.

In contrast to hot rolled FSP, the aged FSP showed significant grain rotation i.e. change in orientation of grain at –M2.4 & –M1.8 Figure 31 (e, f) respectively. At these locations, grains with (0002) orientation decreased & there is increase in the grains with orientation closer to {11-20}. This orientation is quite different with respect to hot rolled FSP.

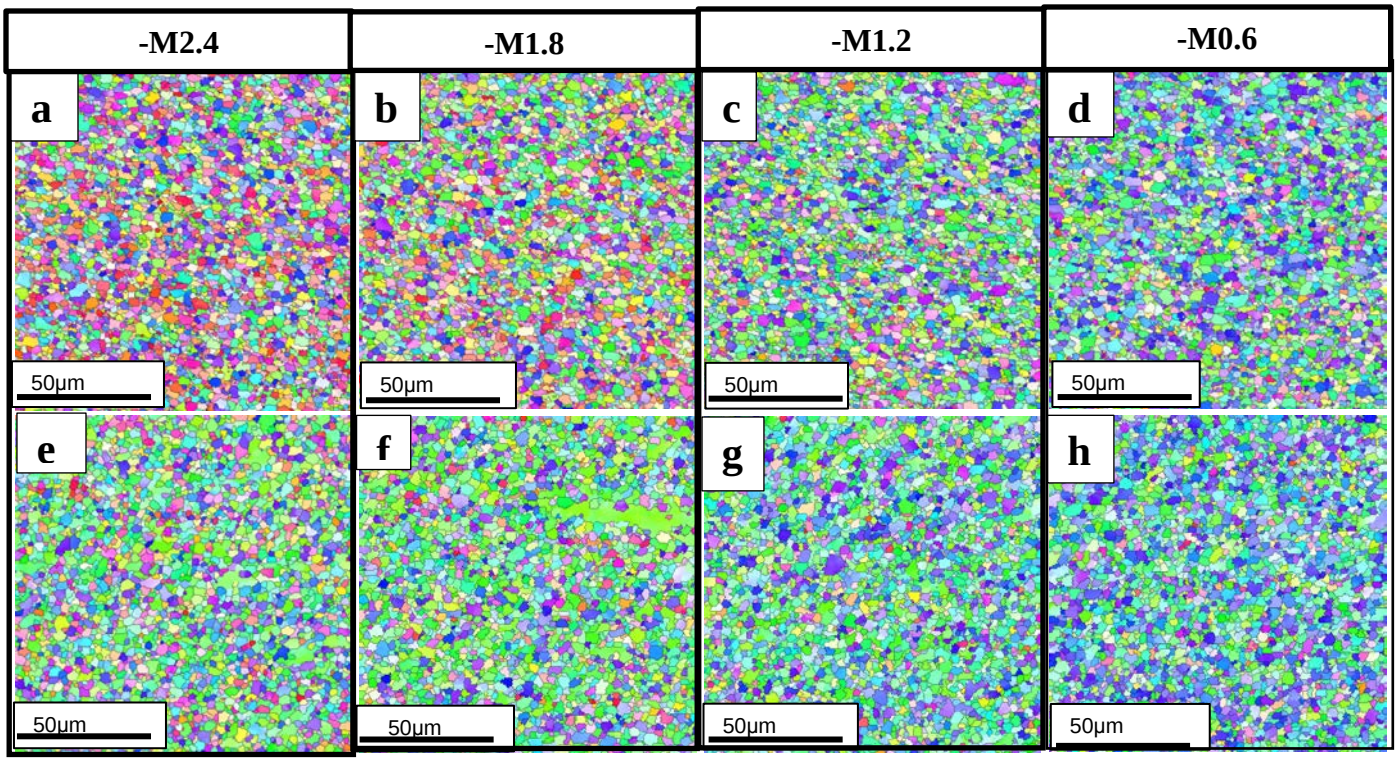

Figure 31 IPF map of retreating side of hot rolled FSP (a) –M2.4 (b) –M1.8 (c) –M1.2 (d) –M0.6 IPF map of retreating side aged FSP (e) –M2.4 (f) –M1.8 (g) –M1.2 (h) –M0.6

5.3.5. IPF Map Of Advancing Side

On the advancing side, an IPF map at +M0.6 & +M1.2 location of hot FSP showed grains with orientation {10-10} & {11-20} Figure 32 (a, b) which, quite similar to the +M0.6 and +M1.2 location of aged FSP Figure 32 (e, f). Apparently, the orientation of grains at the extreme end of advancing side i.e. +M1.8 & +M2.4 are also similar to the extreme end of retreating side i.e. –M1.8 & -M2.4. The orientation of grains at +M1.8 & +M2.4 showed increase in the grains with orientation closer to basal plane i.e. {0002} Figure 32 (c, d). After ageing, there is

significant change in the orientation of grains at +M1.8 & +M2.4 (Figure 32g & 32h) as compared to the hot rolled FSP region at same location. The grains with orientation {11-20} increased with decrease in grain with orientation closer to (0002) (Figure 32g & 32h).

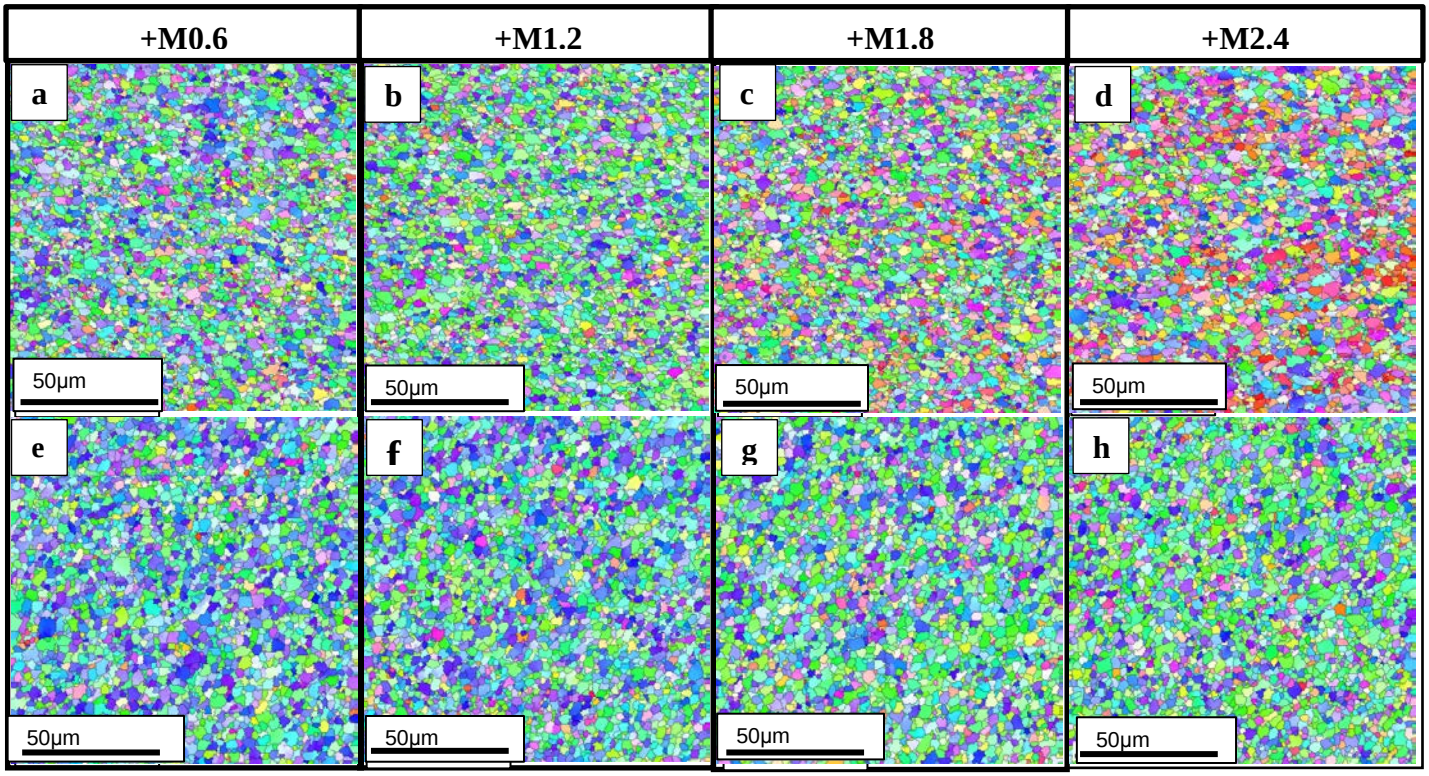

Figure 32 IPF map of retreating side of hot rolled FSP (a) +M0.6 (b) +M1.2 (c) +M1.8 (d) +M2.4 IPF map of retreating side aged FSP (e) +M0.6 (f) +M1.2 (g) +M1.8 (h) +M2.4

5.3.6. Pole Figure {0002} Of FSP

After FSP, weakening of (0002) texture is observed (Figure 33). From –M0.6 to –M2.4 location in the hot rolled FSP, texture intensity of (0002) pole is decreased (Figure 33 (d-a)). It shows that the orientation of (0002) planes were migrated from ~82°- 87° to ~90°- 95° (from –M0.6 to –M2.4). The orientation of (0002) pole at –M2.4 Figure 33 (a) appear in some measure matches with (0002) pole of hot rolled BM seen in Figure 29 (c). On ageing, the texture of (0002) pole on the retreating side is changed to opposite side of pole map from the previous hot rolled FSP. This indicates that there is rotation of grains. As seen in Figures 33 (h–e), there is

increase in the texturing of basal plane texture from –M0.6 to –M2.4. Here also, orientation of (0002) pole at –M2.4 Figure 33 (e) in some measure matches with (0002) pole of aged base material seen in Figure 29(d).

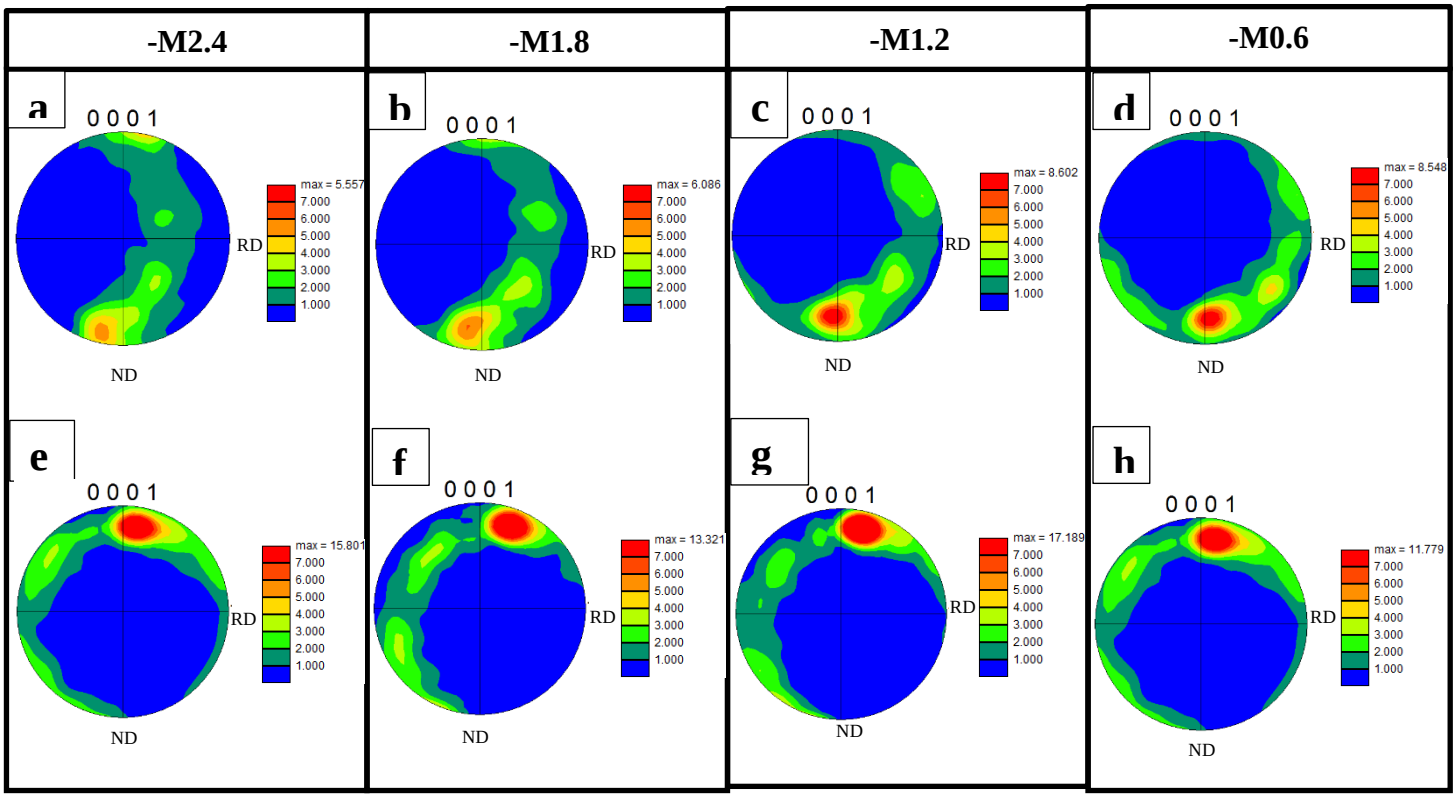

Figure 33 Pole figure of retreating side of hot rolled FSP (a) –M2.4 (b) –M1.8 (c) –M1.2 (d) –M0.6 Pole Figure of retreating side aged FSP (e) –M2.4 (f) –M1.8 (g) –M1.2 (h) –M0.6

On the advancing side of the hot rolled FSP, texture distribution of (0002) pole appears to be different from retreating side of the hot rolled FSP. In case of the hot rolled FSP, the texture of (0002) pole became weak on moving from +M0.6 to +M2.4 fig 34 (a-d). After ageing, texture of (0002) poles is migrated to opposite side of pole map from the texture of hot rolled FSP as seen in Figure fig 34 (e-h). The basal planes are aligned parallel to the rolled surface. On ageing, texture of basal pole did not show any change in FSP region from +M0.6 to +M2.4 (Figure 34).

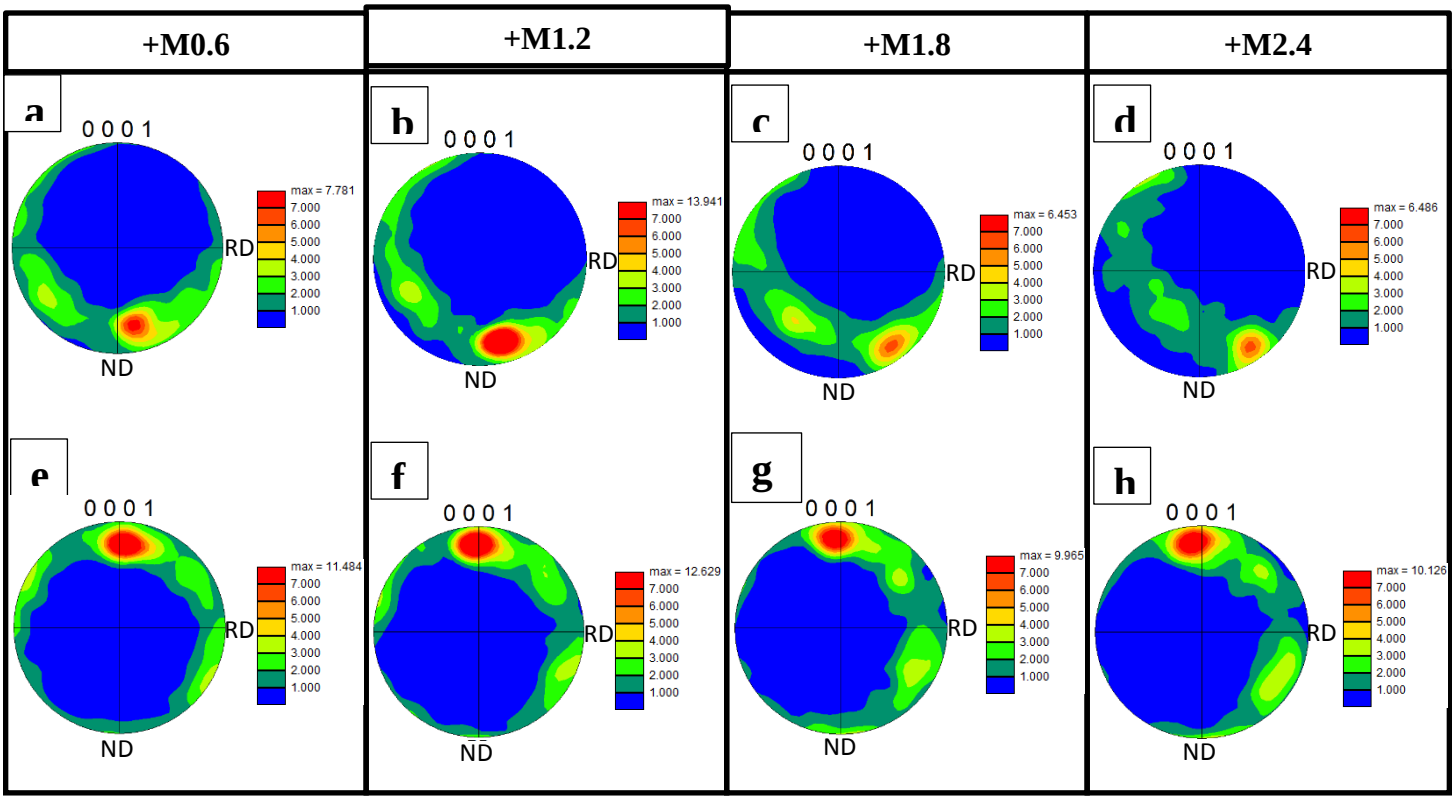

Figure 34 Pole figure of advancing side of hot rolled FSP (a) +M0.6 (b) +M1.2 (c) +M1.8 (d) +M2.4 Pole Figure of advancing side aged FSP (e) +M0.6 (f) +M1.2 (g) +M1.8 (h) +M2.4

5.4. Discussion

Based on the microstructure of hot rolled FSP and aged FSP region (Figure 28c and 28d), it is more clear that volume fraction of precipitates increased significantly in aged FSP sample compared to hot rolled FSP. Even though, intra-granular precipitates were observed in aged FSP that did not see in hot rolled FSP. The WE43 alloy contains Y & RE elements. The addition of Y/RE elements in magnesium alloys causes randomization or weakening of texture during hot working [34, 35, 42, 43]. This alloying element effectively helps in activation of <c+a> slip system due to c/a ratio. Due to activation of <c+a> slip system, basal poles i.e. (0002) rotates toward RD (Figure 29) which matches in previous study [44].

The FSP region showed grains with (10-10) and (11-20) orientation. According to previous study, dynamic recrystallization destroys texture in stir zone, which plastically deformed. The alignment of basal plane normal is roughly surrounding to the rotating tool surface [47].

The both extreme end (±M2.4 and ±M1.8) of hot rolled FSP region showed change in orientation of grains compared to middle part of FSP (±M0.6 and ±1.2) Figure 31 and 32. The influence of thermo-mechanical zone and low temperature at the extreme end of FSP region could have caused change in grain orientation. After ageing, rotations of grain were observed at the extreme end (±M2.4 and ±M1.8) of FSP (Figure 31 and 32). After recrystallization, two mechanism i.e. PSN and solute drag effect may have caused the change in orientation of grain. According to previous literature, the weakening of texture due to PSN in WE43 alloy does not appear to dominate final texture [36]. It can be hypothesized that the solute content in WE43 alloy influences grain boundary behavior and orientation relationship for high boundary mobility [46, 47]. Because of solute drag effect, growth of non-basal grain over basal grain was occurred after FSP and ageing.

5.5. Conclusion

This work demonstrates that ageing of the FSP microstructure causes grain rotation. Such rotation is more prominent towards the center of the FSP region, while the extremities of the FSP nugget experiences relatively grain rotation. This rotation of grain may have occurred due to solute drag effect. The alloying elements of WE43 alloy impact on grain boundary behavior and orientation relationship of high mobility boundary. This effect leads to growth of non-basal grain over basal grain.

CHAPTER 6

SUMMARY

The present work focused at characterization of precipitates exists during isothermal treatment or thermo mechanical treatment in Mg-Nd based alloy. This work involves understanding of precipitate evolution sequence under different thermal or thermo mechanical treatment. The mechanisms involved in precipitation were studied. The applied stress in thermal treatment promotes formation of precipitates that are absent in isothermal treatment. The formations of certain precipitates on dislocation were observed.

The first section involves effect of applied stress at high temperature (creep) on precipitates with respect to isothermal treatment in Mg-Nd alloy. In isothermally annealed sample, localized Nd enriched regions were observed. The β′ precipitates seem to be homogeneously distributed throughout the α-Mg matrix in the creep tested condition. The applied stress promotes the formation of β′ precipitates presumably by reduction of activation barrier for β′ nucleation as well as stress assisted accelerated diffusion of Nd atoms.The β_1 precipitates decorating the dislocation lines were observed in both creep tested and isothermally annealed condition (after 5hrs, 100hrs and 230hrs exposure). The coarser β_1 precipitates were observed in isothermally annealed sample compared to creep sample. After 5 hrs isothermal annealing, the slower nucleation and growth of β′ precipitates in the α-matrix as compared to creep tested sample led to a higher degree of supersaturated Nd solutes retained within the α-matrix which facilitates the faster growth and coarsening of β_1 precipitates. On other hand, rapid rate of nucleation and growth of β′ precipitates in creep tested sample depletes Nd content in the α-matrix which inhibits coarsening of β_1 precipitates.

The second section involves characterization of precipitates in hot rolled WE43 alloy and followed by subsequent ageing. In hot rolled condition, honeycomb like precipitates were formed on subgrain boundaries which became precursors to precipitates formed on subsequent ageing. In aged specimen, well developed honeycomb shaped precipitates were formed. In these precipitates, multiple variants of Nd rich plate shaped β_1 precipitates were connected via Y rich oval shaped β' precipitates.

The last section demonstrates that ageing of the FSP microstructure causes grain rotation. Such rotation is more prominent towards the center of the FSP region, while the extremities of the FSP nugget experiences relatively grain rotation. This rotation of grain may have occurred due to solute drag effect. The alloying elements of WE43 alloy impact on grain boundary behavior and orientation relationship of high mobility boundary. This effect leads to growth of non-basal grain over basal grain.

REFERENCES

[1] Magnesium Die Casting Handbook; NADACA, 1998

[2] Mordike B.L, Ebert T. Materials Sci & Engg A302; (2001); 37-45

[3] Zhu S.M., Gibson M.A., Easton M.A and Nie J.F. Scripta Materialia 63 (2010) 698-703

[4] Polmear I. J.: Physical Metallurgy of Magnesium Alloys, Magnesium alloys and Their Applications, 1992, p. 201

[5] Saito,Kaichi and Hiraga Kenji Metall. Transactions, 52; (2011); 1860-1867.

[6] Nie J.F., Xiao X.L., . Luo C.P, Muddle B.C. Micron 32; (2001); 857-863

[7] Nie J.F. Metallurgical and Materials Transactions A (2012); 49

[8] Miller M.K., Atom Probe Tomography: Analysis at the atomic level, Kluwer Academic/Plenum publishers, New York, 2000

[10] Chia TL, Easton MA, Zhu SM, Gibson MA, Birbilis N, Nie JF. Intermetallics 2009; 17: 481

[11] Easton MA, Gibson MA, Qiu D, Zhu SM, Grobner J, Schmid-Fetzer R, Nie JF , Zhang MX. Acta Mater 2012;60: 4420

[12] Yan J, Sun Y, Xue F, Xue S, Tao W. Mater Sci Eng A 2008; 476: 366

[13] Janik V, Yin DD, Wang QD, He SM, Chen CJ, Boehlert CJ. Mater Sci Eng A 2011; 528: 3105

[14] Ning ZL, Liu HH, Cao FY, Wang ST, Sun JF, Qian M. Mater Sci Eng A 2013; 560: 163

[15] Choudhuri D, Dendge N, Nag S, Gibson MA, Banerjee R. Metall Mater Trans A 2013; 44: 2905

[16] Choudhuri D, Meher S, Nag S, Dendge N, Hwang JY, Banerjee R. Philos Mag Lett 2013; 93: 395

[17] Nie JF, Muddle BC. Acta Mater 2000; 48: 1691

[18] Mengucci P, Barucca G, Riontiono G, Lussana D, Nassazza M, Ferragut R, Aly EH. Mater Sci Eng A 2008; 479: 37

[19] Pike TJ, Noble. J Less-Common Metal 1973; 30: 63

[20] Nie JF. Metall Mater Trans A 2012; 43A: 3891

[21] Gao Y, Liu H, Shi R, Zhou N, Xu Z, Zhu YM, Nie JF, Wang Y. Acta Mater 2012; 60:4819

[22] Lorimer G, Azari-Khosroshahi R and Ahmen M., Japan Institute of Metals; 1999. p.185

[23] Apps P.J., Karimzadeh H., . King J.F and Lorimer G.W., Scripta. Mater. 48(2003) p.475

[24] Antion C., Donnadieu, Perrard F., Deschamps A., Tassin C., and Pisch A., Acta. Mater. 51(2003)p.5335

[25] Barucca G., Ferragut R., Fiori F., Lussana D., Mengucci P., Moia F., and Riontino G., Acta. Mater. 59(2011)p.4151

[26] Nie J.F., Scripta. Mater. 48(2003)p.1009

[27] Roven H.J., M. Liu and Weerenskiold J.C., Mater. Sci. Eng. A 483-484(2008)p.54

[28] Hou X.L, Cao Z.Y., Sun X., Wang L.D. and Wang L.M., J. Alloys. Compd. 525(2012)p.103

[29] Dechamps A., Fribourg G., Brechet Y., Chemin J.L. and Hutchinson C.R., Acta. Mater. 60(2012)p.1905

[30] Wang Y. and Li J., Acta. Mater. 58(2010) p.1212

[31] Ma ZY, Mishra RS, Mahoney MW. Acta Mater 2002;50:4419.

[32] Esparza JA, Davis WC, Trillo EA, Murr LE. J Mater Sci Lett 2002;21:917.

[33] Yi S.B., Bohlen J., Heinemann F., Letzig D., Acta Mater. 58 (2) (2010) 592–605.

[34] Mackenzie L.W.F., Davis B., Humphreys F.J., Lorimer G.W. Mat. Sci. Technol., 23 (10) (2007), pp. 1173–1180

[35] Bohlen J., Nürnberg M.R., Senn J.W., Letzig D., Agnew S.R. Acta Mater., 55 (2007), pp. 2101–2112

[36] Laser T., Hartig Ch., Nürnberg M.R., Letzig D., Bormann R. Acta Mat., 56 (12) (2008), pp. 2791–2798

[37] Hantzsche K., Bohlen J., Wendt J., Kainer K.U., Yi S.B., Letzig D. Scripta Mater., 63 (2010), pp. 725–730

[38] Park S., Sato Y., and Kokawa H. Metall. Mater. Trans. A, 2003, vol 34A, pp. 987-94

[39] Sato Y.S., Kokawa H., Ikeda K., Enomoto M., Jogan S., and Hashimoto T.: *Metall. Mater. Trans. A*, 2001, vol. 32A, pp. 941–48.

[40] A. Couret and D. Caillard: *Acta Metall.*, 1985, vol. 33, pp. 1447–54

[41] Mackenzie L.W.F. and Perkguleryuz M.O. Scripta Mater., 59 (2008), p. 665-668

[42] Hadorn J.P., Hantzsche K., Yi S., Bohlen J., . Letzig D, J.A. Wollmershauser, and Agnew S.R.: *Metall. Mater. Trans. A*, 2012, vol. 43A. pp. 1347-1362

[43] Agnew S.R., Tomé C.N., Yoo M.H. Acta Mater, 49 (2001), pp. 4277–4289

[44] Wang Y.N., Huang J.C. Mater Chem Phys, 81 (2003), p. 11

[45] Humphreys F.J. and Hatherly M. 'Recrystallization and related annealing phenomena', 2nd edn; 2004, Amsterdam, Elsevier

[46] Lücke K., . Detert K Acta Metall, 5 (1957), p. 628

[47] Field D.P., Nelson T.N., Hovanski Y., and Jata K.V: *Metall. Mater. Trans. A*, 2001, vol. 32A, pp. 2869–77.